Monthly Notices of the ROYAL ASTRONOMICAL SOCIETY

MNRAS **522,** 3481–3505 (2023) https://doi.org/10.1093/mnras/stad1171
Advance Access publication 2023 April 24

SN 2021fxy: mid-ultraviolet flux suppression is a common feature of Type Ia supernovae

J. M. DerKacy [1,2★] S. Paugh [1] E. Baron [1,3,4] P. J. Brown [5] C. Ashall [2] C. R. Burns [6] E. Y. Hsiao [7] S. Kumar [7] J. Lu [7] N. Morrell [8] M. M. Phillips [8] M. Shahbandeh [7,9] B. J. Shappee [10] M. D. Stritzinger [11] M. A. Tucker [12,13,14] Z. Yarbrough [1,15] K. Boutsia [8] P. Hoeflich [7] L. Wang [5] L. Galbany [16,17] E. Karamehmetoglu [11] K. Krisciunas [5] P. Mazzali [18] A. L. Piro [6] N. B. Suntzeff [5] A. Fiore [19,20,21] C. P. Gutiérrez [22,23] P. Lundqvist [24] and A. Reguitti [21,25,26]

Affiliations are listed at the end of the paper

Accepted 2023 April 14. Received 2023 April 7; in original form 2022 October 27

ABSTRACT

We present ultraviolet (UV) to near-infrared (NIR) observations and analysis of the nearby Type Ia supernova SN 2021fxy. Our observations include UV photometry from *Swift*/UVOT, UV spectroscopy from *HST*/STIS, and high-cadence optical photometry with the Swope 1-m telescope capturing intranight rises during the early light curve. Early $B - V$ colours show SN 2021fxy is the first 'shallow-silicon' (SS) SN Ia to follow a red-to-blue evolution, compared to other SS objects which show blue colours from the earliest observations. Comparisons to other spectroscopically normal SNe Ia with *HST* UV spectra reveal SN 2021fxy is one of several SNe Ia with flux suppression in the mid-UV. These SNe also show blueshifted mid-UV spectral features and strong high-velocity Ca II features. One possible origin of this mid-UV suppression is the increased effective opacity in the UV due to increased line blanketing from high velocity material, but differences in the explosion mechanism cannot be ruled out. Among SNe Ia with mid-UV suppression, SNe 2021fxy and 2017erp show substantial similarities in their optical properties despite belonging to different Branch subgroups, and UV flux differences of the same order as those found between SNe 2011fe and 2011by. Differential comparisons to multiple sets of synthetic SN Ia UV spectra reveal this UV flux difference likely originates from a luminosity difference between SNe 2021fxy and 2017erp, and not differing progenitor metallicities as suggested for SNe 2011by and 2011fe. These comparisons illustrate the complicated nature of UV spectral formation, and the need for more UV spectra to determine the physical source of SNe Ia UV diversity.

Key words: supernovae: general – supernovae: individual: SN 2021fxy, SN 2013dy, SN 2017erp, ASASSN-14lp.

1 INTRODUCTION

Type Ia supernovae (SNe Ia) are important astrophysical objects because of their utility as 'standardizable candles' for cosmological studies. The empirical Phillips relation (Phillips 1993; Phillips et al. 1999) allows them to serve as cosmological probes, revealing the accelerating expansion rate of the universe (Riess et al. 1998; Perlmutter et al. 1999).

While it is well established that SNe Ia are explosions of a primary carbon and oxygen (C/O) white dwarves in binary systems (Hoyle & Fowler 1960), the full nature of the progenitor system, including the identity of the secondary star and the explosion mechanism, are still unclear (for a review see Maoz, Mannucci & Nelemans 2014). In the single-degenerate (SD) scenario, the companion is either a main-sequence star or an evolved, non-degenerate companion like a red giant or He-star (Whelan & Iben 1973). In the double-degenerate (DD) scenario, the companion is also a white dwarf, where the explosion is triggered by the merger or interaction of the two WDs (Iben & Tutukov 1984; Webbink 1984). More recent work has suggested that some SNe Ia may potentially originate from the merger of a WD with the core of an evolved star; known as the core-degenerate scenario (Kashi & Soker 2011; Soker, García-Berro & Althaus 2014). A wide range of explosion mechanisms have been proposed, including pure deflagrations (Nomoto, Thielemann & Yokoi 1984), detonation-to-deflagration transitions (DDTs; also referred to as delayed detonations) (Hoeflich, Khokhlov & Wheeler 1995; Höflich & Stein 2002; Höflich 2006), surface helium detonations (Thielemann, Nomoto & Yokoi 1986; Woosley & Weaver 1994; Livne & Arnett 1995; Shen et al. 2018; Polin, Nugent & Kasen 2019), and detonations triggered by the 'violent' mergers of two WDs before they are able to fully merge (Rosswog et al. 2009; Pakmor et al. 2010, 2012). There is no consensus as to whether SNe Ia occur by any or all of these proposed mechanisms, making the SNe Ia progenitor/explosion mechanism problem extremely complex.

Several different schemes have been developed to characterize the observed diversity of SNe Ia near maximum light. Branch et al. (2006) subdivide SNe Ia into four groups: core-normal (CN), shallow silicon (SS), broad line (BL), and cool (CL); based upon the pseudo-equivalent widths (pEWs) of the Si II λ5972 and λ6355 lines in their

★ E-mail: jmderkacy@vt.edu

spectra near maximum light. Recent work with larger samples have shown these groups to be statistically robust (Burrow et al. 2020) and are potentially related to differences in the progenitor systems and/or explosion mechanisms (Polin et al. 2019). Wang et al. (2009) divide SNe Ia into 'Normal' and 'High Velocity (HV)' groups based on the velocity of the Si II λ6355 absorption minimum near *B*-band maximum light, with the HV objects showing redder $B - V$ colours and less scatter in peak luminosity and luminosity decline rate (Δm_{15}) relative to Normal SNe Ia. Benetti et al. (2005) divide the SNe Ia population into 'Faint', 'Low Velocity Gradient' and 'High Velocity Gradient' groupings based on the combination of their decline rate in *B* band and the rate of change in their Si II velocities.

Early observations are key to determining the connections between the observed SNe Ia diversity and different progenitor scenarios and explosion mechanisms. Early observations can probe the physical properties of the system, including constraints on the size of the WD progenitor (Piro, Chang & Weinberg 2010; Nugent et al. 2011; Bloom et al. 2012), the properties of secondary star (Kasen 2010; Maeda, Kutsuna & Shigeyama 2014), and the distribution of any circumstellar material (CSM; Lundqvist et al. 2020). Early photometric observations of nearby SNe Ia discovered within hours of explosion reveal that some SNe Ia (such as SNe 2017cbv, 2018oh/ASASSN-18bt, 2019np, and 2021aefx) show an early excess or 'blue bump' at early times (Hosseinzadeh et al. 2017; Li et al. 2019; Ashall et al. 2022; Hosseinzadeh et al. 2022; Sai et al. 2022). However, there are multiple potential origins of these early-time excesses, including outward mixing of ^{56}Ni in the ejecta (Piro & Morozova 2016; Shappee et al. 2019), production of radioactive material in the detonation of the helium shell (Dimitriadis et al. 2019; Polin et al. 2019), interaction with the companion (Kasen 2010; Maeda et al. 2014; Dimitriadis et al. 2019), and rapid velocity evolution of broad, high-velocity spectroscopic features (Ashall et al. 2022). Attempts to probe the companion interaction in the radio have yet to detect a companion interaction, but have yielded information on the nearby circumstellar environment in the first days after explosion and provided constraints on the wind properties of the progenitor (Lundqvist et al. 2020; Hosseinzadeh et al. 2022).

Colour curves derived from photometry of SNe Ia obtained within the first few days after explosion reveal at least two different populations, distinguishable by their $B - V$ behaviour (Stritzinger et al. 2018). Of the two most populous groups, the first exhibits blue colours from the earliest epochs, while the other group starts out red and rapidly becomes bluer, with both groups showing indistinguishable colours roughly 6 d after first light. These groups are not replicated in $g - r$ colours (Bulla et al. 2020). Spectroscopic observations within these first few days after explosion probe the outermost ejecta layers where differences between models of SNe Ia are largest. For example, DDT models show unburned carbon, oxygen, and possibly silicon in the outermost layers (Hoeflich et al. 2017) compared to the large amounts of ^{44}Ti and ^{56}Ni which are the expected by-products of models relying upon surface helium detonations (Jiang et al. 2017). In the models of Polin et al. (2019) these by-products produce significant line blanketing, resulting in red colours at early times. Early spectra often show high-velocity features (HVFs), which typically disappear before maximum light but may be ubiquitous among SNe Ia (Mazzali et al. 2005).

SNe Ia diversity increases as one moves from optical to ultraviolet (UV) wavelengths. Photometrically, SNe Ia can be divided into two groups based on their near-UV (NUV) colours; the NUV-blue group, whose members have low velocity gradients of their Si II λ6355 lines and conspicuous C II lines, and the NUV-red class, whose members have more diverse Si II velocity gradients and typically lack the C II lines (Milne et al. 2013). The fraction of events belonging to each group varies by redshift, making it difficult to incorporate UV data of SNe Ia into cosmological analyses (Milne et al. 2015; Brown et al. 2017). Spectroscopically, SNe Ia can show drastic differences in the UV despite being almost identical in the optical and near-infrared (NIR; Foley et al. 2016). The best example of this are the 'twin' SNe 2011by and 2011fe (Foley & Kirshner 2013).

Theoretical efforts to better understand UV spectral formation have focused on the impacts of three key variables: (1) metallicity – increases in the progenitor metallicity strengthen line blanketing in the UV and result in lower fluxes (Lentz et al. 2000), (2) density structure – shallower density profiles produce UV spectra with lower flux values and fewer features (Sauer et al. 2008; Hachinger et al. 2013; Mazzali et al. 2014), and (3) luminosity – which induces temperature variations that change both the shape of the underlying continuum and the strength, shape, and location of spectral features (Walker et al. 2012; DerKacy et al. 2020).

In this work, we present observations and analysis of SN 2021fxy, an NUV-red SN Ia discovered roughly 2 d after explosion and for which we obtained multiple *HST*/STIS UV spectra in addition to a comprehensive multiband follow-up effort by the Precision Observations of Infant Supernova Explosions (POISE; Burns et al. 2021) collaboration. Section 2 details these photometric and spectroscopic follow-up observations, followed by a detailed analysis in Section 3, including comparisons to the sample of spectroscopically normal SNe Ia with *HST* UV spectra near maximum light. In Section 4, we compare SNe 2021fxy and 2017erp, both of which are well-observed NUV-red SNe Ia with *HST*/STIS spectra, and who show nearly identical optical properties. We discuss the potential causes of their observed differences in the context of the UV diversity of SNe Ia and what they reveal about the origins of this diversity. We summarize our conclusions in Section 5.

2 OBSERVATIONS

2.1 Discovery

SN 2021fxy was discovered on 2021 March 17.75 by Koichi Itagaki at $m = 16.9$ mag in a clear filter (Itagaki 2021), and classified as a young SN Ia the following night (Jha et al. 2021). SN 2021fxy is located at $\alpha = 13^{\rm h}13^{\rm m}01\overset{\rm s}{.}570$, $\delta = -19°30'45\overset{''}{.}18$, which is $19\overset{''}{.}8$ North and $8\overset{''}{.}1$ East from the centre of the host galaxy, NGC 5018 (see Fig. 1). The most constraining last non-detection comes from ASAS-SN on 2021 March 15.45 in the *g* band at $g > 18.01$ mag, which was retrieved from the ASAS-SN Sky Patrol Database[1] (Shappee et al. 2014; Kochanek et al. 2017). This implies SN 2021fxy was discovered no later than 2.27 d after explosion, assuming there is no dark phase.

NGC 5018 is classified as an E3 according to de Vaucouleurs et al. (1991), at a redshift $z = 0.0094$ (Rothberg & Joseph 2006). Correcting the velocities for local motions based on Mould et al. (2000) and assuming a $H_0 = 73$ km s^{-1} Mpc^{-1} (Riess et al. 2022), this redshift results in a Hubble flow distance of 38.4 ± 2.7 Mpc, corresponding to a distance modulus of $(m–M) = 32.92 \pm 0.15$ mag. SN 2021fxy is at least the second SNe Ia discovered in NGC 5018, along with the well-studied 02bo-like SN 2002dj (Pignata et al. 2008). Another potential SN Ia sibling, SN 2017isq, was discovered roughly one month after maximum light at an estimated separation of 30 kpc from NGC 5018; its closest potential host (Benetti et al. 2017; Tonry et al. 2017). Important information on SN 2021fxy and NGC 5018 can be found in Table 1.

[1] https://asas-sn.osu.edu/

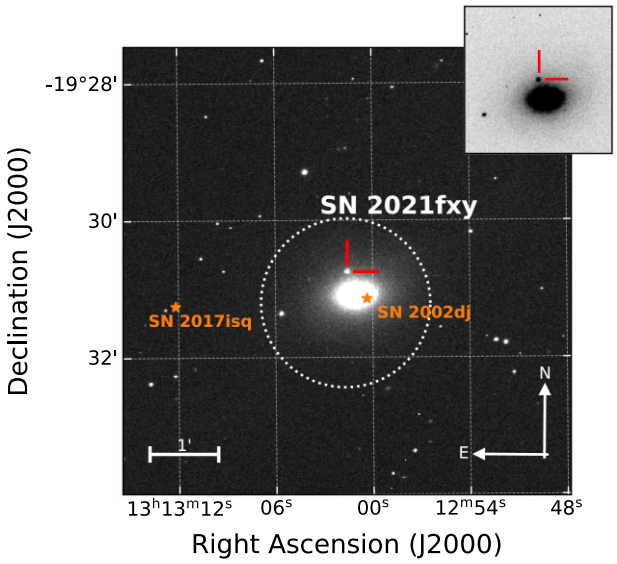

Figure 1. An *r*-band image of NGC 5018 taken the night of 2021-03-24 with the Swope 1-m telescope at Las Campanas Observatory, Chile. SN 2021fxy is highlighted in both the main panel and the false-colour inset with the red cross-hairs. The orange stars indicate the locations of sibling SN 2002dj and potential sibling SN 2017isq.

Table 1. Properties of SN 2021fxy and NGC 5018.

Parameter	Value	Source
SN 2021fxy		
RA [J2000]	$13^{h}13^{m}01\overset{s}{.}570$	(1)
Dec. [J2000]	$-19°30'45\overset{''}{.}18$	(1)
$t(B_{max})$ [MJD]	59305.12 ± 0.34	This work
B_{max} (mag)[a]	13.56 ± 0.07	This work
$E(B-V)_{MW}$ (mag)	0.084	(2)
$E(B-V)_{Host}$ (mag)	0.02 ± 0.06	This work
s_{BV}	0.99 ± 0.03	This work
$\Delta m_{15}(B)$ (mag)[b]	1.05 ± 0.06	This work
NGC 5018		
RA [J2000]	$13^{h}13^{m}01\overset{s}{.}70$	(3)
Dec. [J2000]	$-19°31'12\overset{''}{.}8$	(3)
Morphology	E3	(4)
HV	2816 ± 1	(3)
v (km s^{-1})		
z	0.0094	(3)
μ	32.92 ± 0.15	(3)

[a]Apparent magnitude, corrected for extinction.
[b]Value from `SNooPy` fit with `EBV_model2` to SN 2021fxy light curve.
References – (1) Itagaki (2021), (2) Schlafly & Finkbeiner (2011), (3) Rothberg & Joseph (2006), and (4) de Vaucouleurs et al. (1991).

2.2 Photometric follow-up

2.2.1 *Ground-based photometry*

The POISE collaboration began a multi-band (*uBVgri*) follow-up campaign of SN 2021fxy using the Swope 1-m telescope at Las Campanas Observatory at 2021 March 18.11, just 0.39 d after discovery, placing our first observations no later than 2.66 d after last non-detection. During the early rise, two sets of observations were taken per night to capture rapid, intranight evolution. Roughly one week after discovery, the cadence was reduced to one set of observations per night. Observations from the Swope were reduced and analysed according to the procedures of Krisciunas et al. (2017) and Phillips et al. (2019).

Some post-maximum photometric observations in *BVgri* bands were taken using the Las Cumbres Observatory global 1-m telescope network (LCOGT) as part of the Aarhus-Barcelona FLOWS project.[2] This data was reduced with the BANZAI pipeline (McCully et al. 2018) and calibrated using the local sequence photometry from the Swope observations, assuming zero colour terms.

Photometry obtained from both telescopes are presented in the CSP-II natural system in Section A. For data obtained with the Swope 1-m, S-corrections (Stritzinger et al. 2002) between the CSP-II and CSP-I systems are quite small ($\lesssim$0.01 mag) in all but the *u* band, and are smaller than the typical photometric uncertainty in all bands. Therefore, we conclude that the CSP-I and CSP-II systems are effectively the same (only the CCD was changed between the two projects; Phillips et al. 2019, Suntzeff et al., in preparation). Similarly, because the data obtained with the LCOGT network were calibrated using local sequence photometry from the Swope images, its natural system will be only marginally different than CSP-II; and we therefore treat the data as it if is on the CSP-II system. Unaccounted for errors between the LCOGT natural system and the CSP-II system arising from slightly different photometric transmission functions and differences between individual telescopes within the LCOGT network are expected to be small ($\lesssim$ 3 per cent).

2.2.2 Swift *photometry*

Swift observations were first triggered as part of the *Swift* GI program 'Maximizing Swift's Impact With The Global Supernova Project' (PI: Howell). Observations began on 2021 March 18.25 (2.80 d after last non-detection). Due to the brightness of the underlying host galaxy, some optical observations were made in a hardware mode with a faster readout to reduce the effect of coincidence loss. Photometry was computed with the Swift Optical Ultraviolet Supernova Archive (SOUSA; Brown et al. 2014) pipeline using the 2020 update to the time-dependent sensitivity and aperture corrections calculated in 2021. No subtraction of the host-galaxy flux has been performed due to the lack of pre-explosion images.

2.3 Spectroscopic follow-up

2.3.1 *Optical spectroscopy*

Optical spectroscopic follow-up observations, covering −5.9 d to +45.4 rest frame days relative to *B*-band maximum were made with a global network of telescopes and instruments, including the Dual Imaging Spectrgrpah (DIS) on the Astrophysical Research Consortium 3.5-m telescope at Apache Point Observatory (ARC 3.5-m), ALFOSC on the Nordic Optical Telescope (NOT) by the NUTS2 collaboration[3], the Supernova Integral Field Spectrogaph (SNIFS; Lantz et al. 2004) on the University of Hawaii 2.2-meter telescope (UH88), and both the Magellan Inamori Kyocera Echelle (MIKE) and the Low Dispersion Survey Spectrograph (LDSS3) instruments on the Landon T. Clay (Magellan) Telescope at Las Campanas Observatory. A classification spectrum taken with the Robert Stobie Spectrograph (RSS) on the South African Large Telescope (SALT)

[2]https://flows.phys.au.dk/
[3]https://nuts.sn.ie/

Table 2. Log of spectroscopic observations.

Date (UT)	MJD	Epoch[a]	Obs. Range (Å)	Telescope/Instrument
		Ultraviolet spectra		
2021 Mar 29.8	59302.83	−2.3	1600–5600	*HST*/STIS
2021 Apr 01.6	59305.55	+0.4	1600–5600	*HST*/STIS
2021 Apr 08.4	59312.43	+7.2	1600–5600	*HST*/STIS
		Optical spectra		
2021 Mar 18.1	59291.11	−13.9	3496–9372	SALT/RSS[b]
2021 Mar 25.1	59299.09	−5.9	3398–9674	NOT/ALFOSC
2021 Apr 02.4	59306.38	+1.3	3400–9840	ARC/DIS
2021 Apr 03.1	59307.05	+2.0	3397–9673	NOT/ALFOSC
2021 Apr 04.3	59308.30	+3.2	3400–9840	ARC/DIS
2021 Apr 06.2	59310.21	+5.1	3400–9840	ARC/DIS
2021 Apr 08.5	59312.49	+7.3	3787–9100	UH88/SNIFS
2021 Apr 12.1	59316.11	+10.9	3400–9683	NOT/ALFOSC
2021 Apr 13.3	59317.31	+12.1	3400–9864	ARC/DIS
2021 Apr 17.1	59321.13	+15.9	3439–9412	Magellan (Clay)/MIKE
2021 Apr 17.2	59321.24	+16.0	3816–10632	Magellan (Clay)/LDSS3
2021 Apr 20.0	59324.04	+18.7	3401–9639	NOT/ALFOSC
2021 Apr 20.1	59324.11	+18.9	3707–9290	Magellan (Clay)/LDSS3
2021 May 03.9	59337.93	+32.5	3398–9653	NOT/ALFOSC
2021 May 16.9	59350.91	+45.4	3689–9687	NOT/ALFOSC
		Near-infrared spectra		
2021 Apr 02.4	59306.43	+1.3	6905–25701	IRTF/SpeX
2021 Apr 19.6	59323.56	+18.2	6909–25714	IRTF/SpeX
2021 May 10.2	59344.24	+38.7	6868–25384	IRTF/SpeX

[a]Rest frame days relative to *B*-band maximum of MJD = 59305.12.
[b]Retrieved from TNS (Jha et al. 2021).

at −13.9 d was retrieved from Transient Name Server[4] and is also included here (Jha et al. 2021).

Spectra taken with the ARC 3.5-m were reduced using standard IRAF[5] (Tody 1986, Tody 1993) methods including bias subtraction, flat fielding, cosmic ray removal using L.A. Cosmic[6] package (van Dokkum 2001), and flux calibration from a spectrophotometric standard star taken at a similar airmass that same night. The SNIFS spectrum is traced, extracted, and calibrated with custom PYTHON routines (Tucker et al. 2022) and atmospheric attenuation is corrected using the results of Buton et al. (2013). The spectrum taken with Magellan/MIKE was processed through a combination of IRAF echelle tasks and the 'mtools'[7] package, specially developed for the reduction of MIKE spectra. A flux standard obtained during the same night of the observations was used as flux calibrator. Flux calibration was also checked with a low resolution Magellan/LDSS3 spectrum of SN 2021fxy obtained during the same night as the MIKE observation.

2.3.2 *HST spectroscopy*

UV spectroscopy of SN 2021fxy with the *Hubble Space Telescope* (*HST*) equipped with the Space Telescope Imaging Spectrograph (STIS) using the mid-UV G230L and the near-UV/optical G430L gratings was triggered by the program 'Red or Reddened Supernovae? Understanding the Ultraviolet Differences of Normal Standard Candles' (PI: Brown; ID: 16221). Observations were scheduled for 29/30 March, 01 April, 03 April, and 08 April. Some observations on 01 April and all 03 April were unusable because of a guide star acquisition failure. Reduced spectra were obtained from the Mikulski Archive for Space Telescopes (MAST[8]). The multiple spectra from both grisms were combined using a weighted average within a bin of 5 Å.

2.3.3 *NIR spectroscopy*

The NIR spectra of SN 2021fxy were obtained with the SpeX (Rayner et al. 2003) spectrograph installed on the 3.0-m NASA Infrared Telescope Facility (IRTF) on three epochs (2021-04-02, 2021-04-19, and 2021-05-10). The spectra were taken in both the PRISM and SXD mode with a slit size of 0.5 × 15 arcsec^2. The spectra were taken using the classic ABBA technique, and were reduced utilizing the `Spextool` software package (Cushing, Vacca & Rayner 2004). The telluric absorption corrections were done using the `XTELLCOR` software. Complete details of the reduction procedure can be found in Hsiao et al. (2019). The complete log of spectroscopic observations is given in Table 2.

[4]https://www.wis-tns.org/
[5]IRAF is distributed by the National Optical Astronomy Observatories, which are operated by the Association of Universities for Research in Astronomy, Inc., under cooperative agreement with the National Science Foundation (NSF).
[6]http://www.astro.yale.edu/dokkum/lacosmic/
[7]http://www.lco.cl/?epkb_post_type_1 = iraf-mtools-package
[8]https://science.nasa.gov/astrophysics/astrophysics-data-centers/multimission- archive-at-stsci-mast

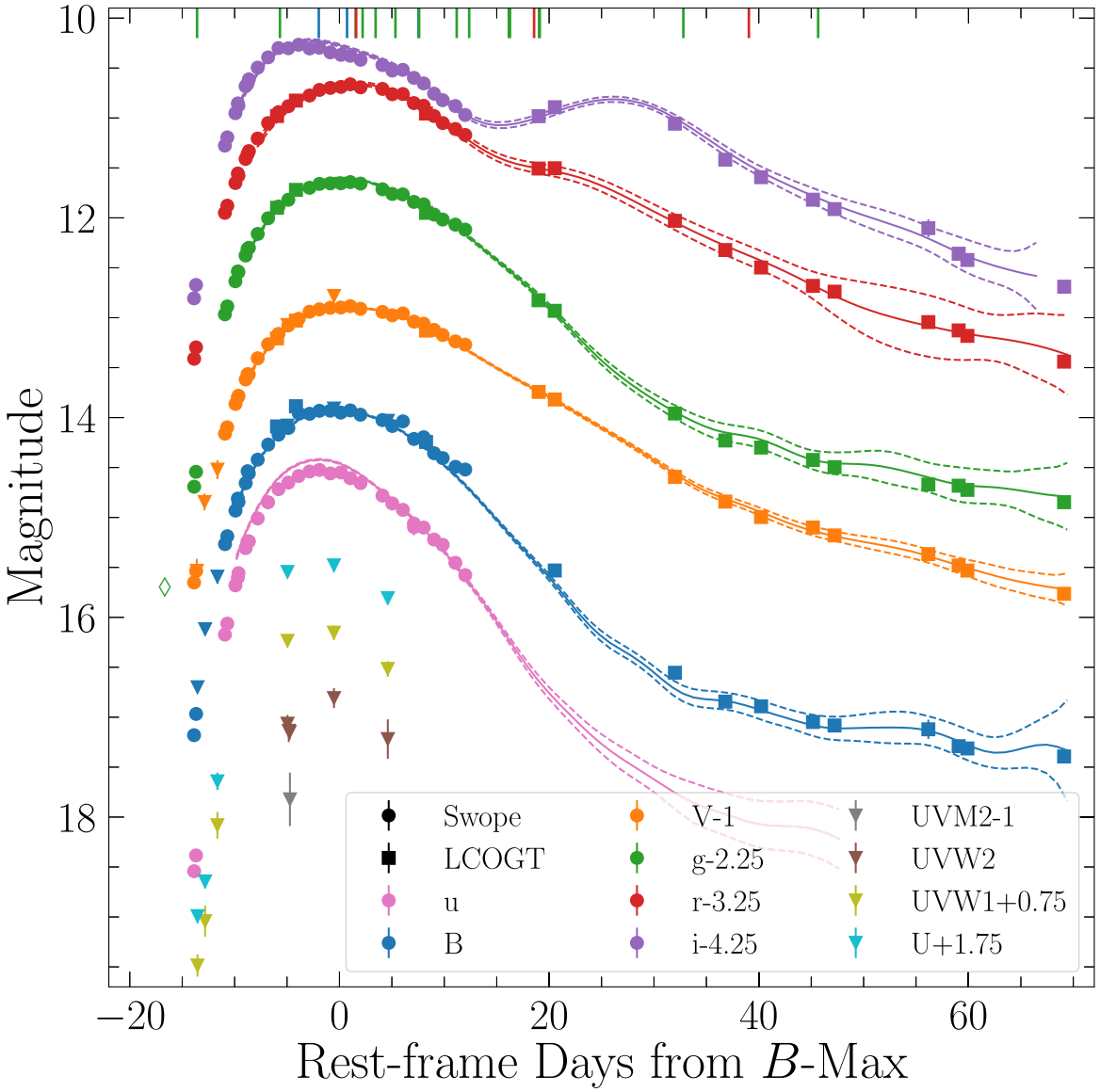

Figure 2. Multiband light curves of SN 2021fxy. *uBVgri* data from the Swope 1-m telescope are shown in circles, *BVgri* data from Las Cumbres Observatory Global Telescope 1-m network in squares, and *UVW*2, *UVM*2, *UVW*1, *U*, and *B* data from *SWIFT/UVOT* in triangles. The last non-detection from ASAS-SN is noted with an open diamond. Rest-frame epochs of UV (blue), optical (green), and NIR (red) spectra are marked along the top axis. `SNooPy` fits to the *uBVgri* photometry are plotted (solid lines), with 1σ errors (dashed lines).

3 ANALYSIS

3.1 Light-curve analysis

The full multiband light curves are shown in Fig. 2, with the *uBVgri* photometry presented in the CSP natural system. Using SuperNovae in Object Oriented Python (`SNooPy`; Burns et al. 2014), we fit the *uBVgri* light curves with the `EBV_model2`, with the fits shown in Fig. 2. From the fit, we measure a *B*-band maximum of 13.57 ± 0.01 mag on $t_{\rm max} = 59305.12 \pm 0.34$ d, corresponding to 16.7 d after last non-detection. The colour-stretch $s_{\rm BV}$ is found to be 0.99 ± 0.03, which is consistent with a normal-bright SN Ia. We obtain a value of $\Delta m_{15}(B) = 1.05 \pm 0.06$ mag from the `SNooPy` fit to the multiband light curves. The distance modulus is estimated from our fit as $\mu = 32.86 \pm 0.08$ mag, which is consistent with the value derived from the host redshift in Section 2. The host extinction derived from the SN light curves is estimated to be $E(B-V)_{\rm host} = 0.02 \pm 0.06$ mag. Attempts to constrain the time of explosion from the early light curve were unsuccessful due to an insufficient number of photometric observations resulting from a three day gap after the first night of follow-up.

An examination of the early $B-V$ colour evolution, as shown in Fig. 3, reveals that SN 2021fxy follows the 'red' evolutionary track, as defined by Stritzinger et al. (2018). SN 2021fxy's classification as a 'shallow-silicon' (SS) object within the Branch scheme (see Section 3.2) would make it the first known spectroscopically normal SS object to follow the 'red' track[9] as all the normal SS/91T-

[9]Stritzinger et al. (2018), Contreras et al. (2018), and Cain et al. (2018) describe SN 2012fr as a spectroscopically peculiar SN Ia lying on the border of the CN/SS subgroups, which follows the 'red' evolutionary track. Burrow et al. (2020) found that SN 2012fr had a 98.5 per cent probability of being a SS object.

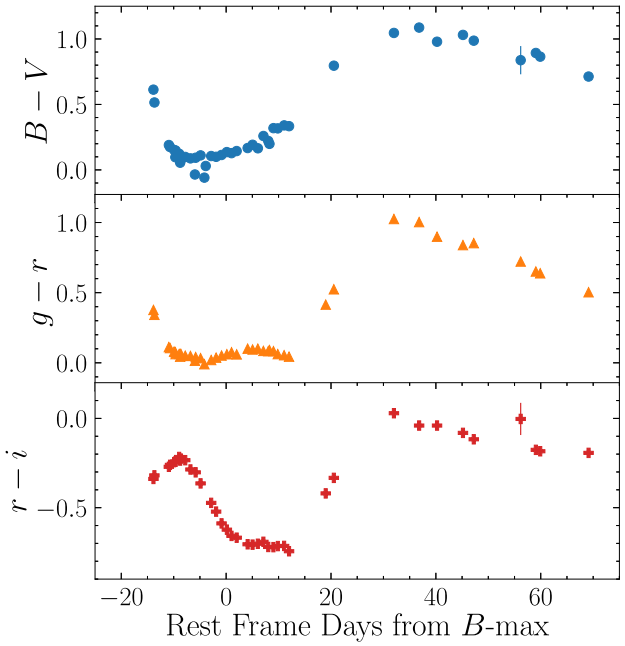

Figure 3. $B - V$, $g - r$, and $r - i$ colour curves of SN 2021fxy in the CSP natural system.

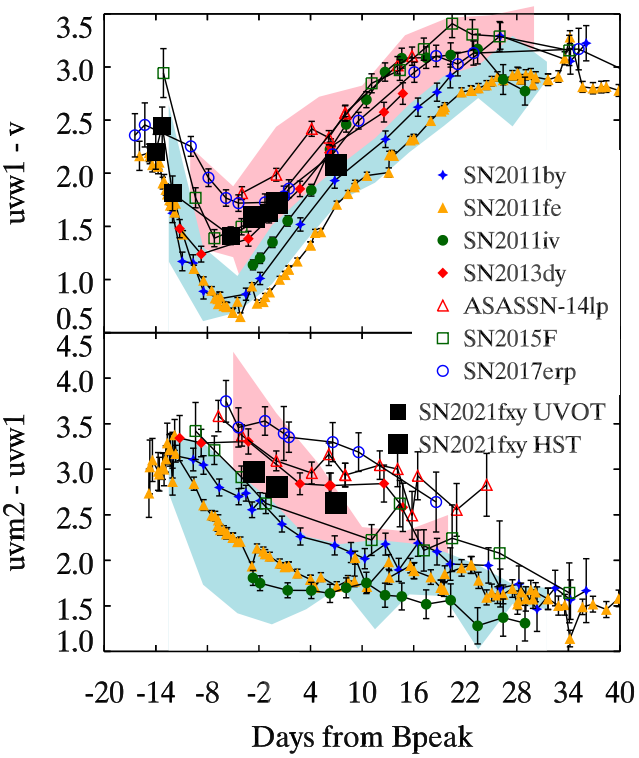

Figure 4. UV colour evolution of SN 2021fxy compared to other spectroscopically normal SNe Ia with *HST* UV spectroscopy. The pale blue and red polygons note the locations of NUV-blue and NUV-red objects, respectively, as defined in Milne et al. (2013). The larger black squares are synthetic measurements derived from *HST*/STIS UV spectral observations of SN 2021fxy and the *Swift/UVOT* filters (Breeveld et al. 2011).

like objects in the Stritzinger et al. (2018) sample follow the 'blue' track.

The colour evolution in the UV compared to other SNe Ia with *HST* UV spectroscopy is shown in Fig. 4. To supplement the low number of *Swift* observations, we compute synthetic photometry using the *HST*/STIS spectra and the *Swift*/UVOT filters as calibrated by Breeveld et al. (2011). The agreement of *Swift*/UVOT photometry and spectrophotometry from *HST* spectra has been found to agree at the 0.05 mag level (Brown et al. 2014). SN 2021fxy is found to be an NUV-red object in the Milne et al. (2013) scheme, and shows evolution similar to other NUV-red objects SNe 2013dy, ASASSN-14lp, and 2017erp.

3.2 Spectroscopic analysis

3.2.1 Optical spectra

The optical spectral sequence of SN 2021fxy is shown in Fig. 5. The earliest optical spectrum at −13.9 d relative to *B*-band maximum shows both high velocity Si II λ6355 and Ca II NIR triplet features at −18 200 and −27 400 km s^{-1}, respectively, as measured from the minimum of the absorption troughs. Using the blue edge of the absorption troughs as a measure of the maximal velocity extent of the line-forming ejecta, we estimate the Si IIλ6355 line extends to at least −28 000 km s^{-1}, while the Ca II extends to at least −40 000 km s^{-1}; although strong telluric features and possible blending make identification of this edge difficult. At −5.9 d, the high velocity Si II has mostly faded, but can still be detected to roughly −21 000 km s^{-1}. Meanwhile the high velocity Ca II remains prominent, particularly in the NIR triplet, until roughly +12 d, before fully disappearing around +19 d. In the −5.9-d spectrum, material in both the H&K lines and the NIR triplet extend to −29 000 km s^{-1}. The Si II λ6355 line has a noticeably flat emission peak, indicating that the Si is detached from the photosphere (Jeffery & Branch 1990).

The spectra otherwise resemble that of a typical 'Branch-normal' SN Ia, as shown in Fig. 6.

A high-resolution spectra at +15.9 days taken with the MIKE spectrograph on the Landon T. Clay (Magellan) telescope reveals four distinct Na I D doublets along the line of sight to the supernova in the Milky Way (see Fig. 7). The pseudo-equivalent width of the Galactic Na I D lines is 0.524 ± 0.002 Å, which implies an extinction of $E(B - V)_{MW} = 0.058 \pm 0.039$ mag according to eq. (9) of Poznanski, Prochaska & Bloom (2012), compared to the $E(B - V)_{MW} = 0.084$ mag derived from the Schlafly & Finkbeiner (2011) re-calibration of the Schlegel, Finkbeiner & Davis (1998) dust maps, assuming $R_V = 3.1$. Note that, Phillips et al. (2013) found that Poznanski et al. (2012) had underestimated their errors by about a factor of three, thus the two values are consistent with each other. No absorption from Na I D is seen at or near the redshift of NGC 5018, implying that there is negligible host reddening of SN 2021fxy (Phillips et al. 2013); consistent with a host galaxy of type E3 and the estimate derived from the SN photometry.

Velocity measurements of several key SN Ia features were made using the Measure Intricate Spectral Features In Transient Spectra (`misfits`) package[10] (Holmbo 2020) and are shown in Fig. 8. Fitted spectra are first smoothed using the Fast Fourier Transform low-pass filter method described in Marion et al. (2009). Next, a raw error spectrum is calculated from the difference between the unsmoothed and smoothed spectra, before it is smoothed using a Gaussian kernel.

[10] https://github.com/sholmbo/misfits

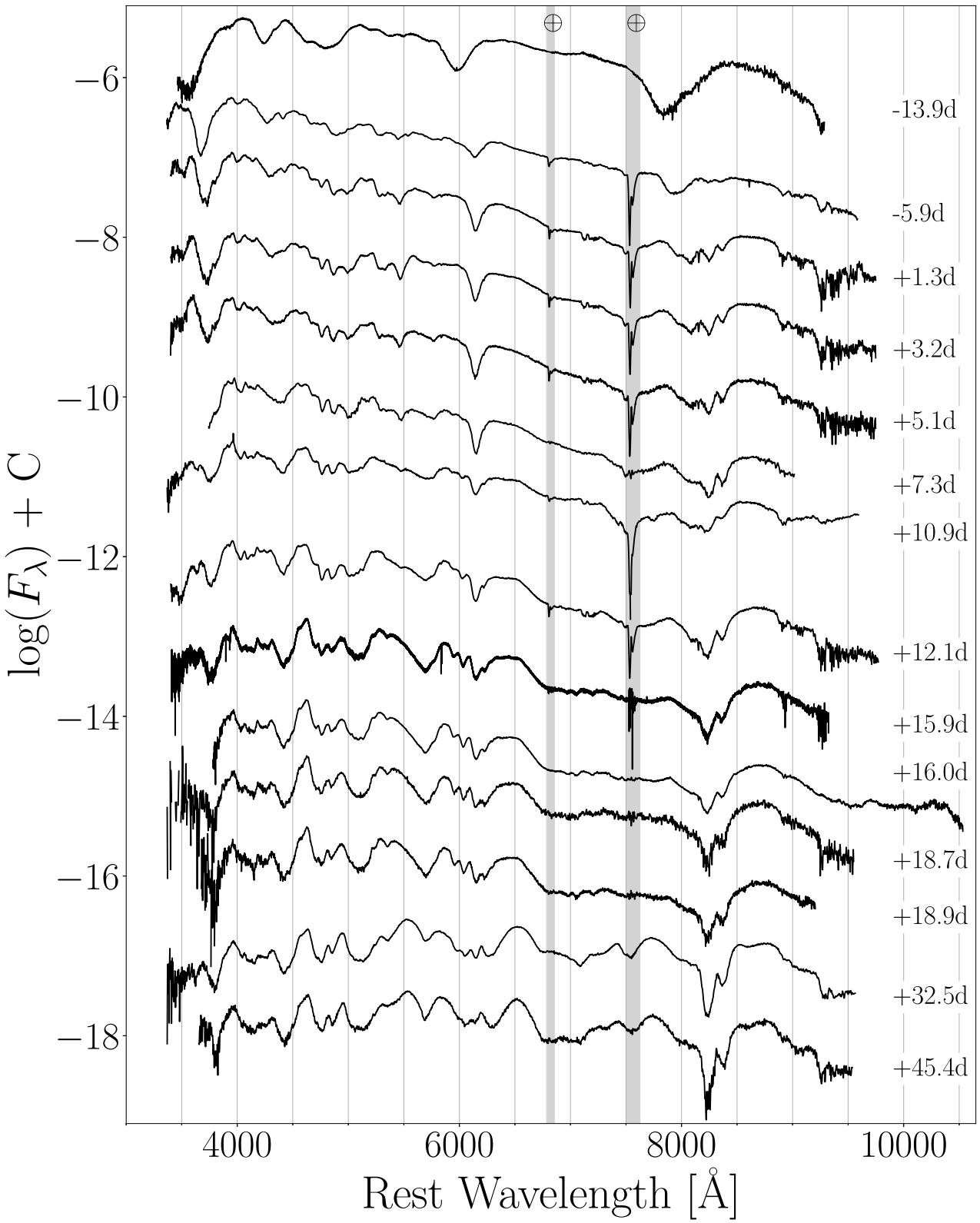

Figure 5. Optical spectra of SN 2021fxy corrected for Milky Way extinction. Epoch relative to rest-frame *B*-band maximum are shown next to each spectrum. Grey boxes mark regions of strong telluric absorption.

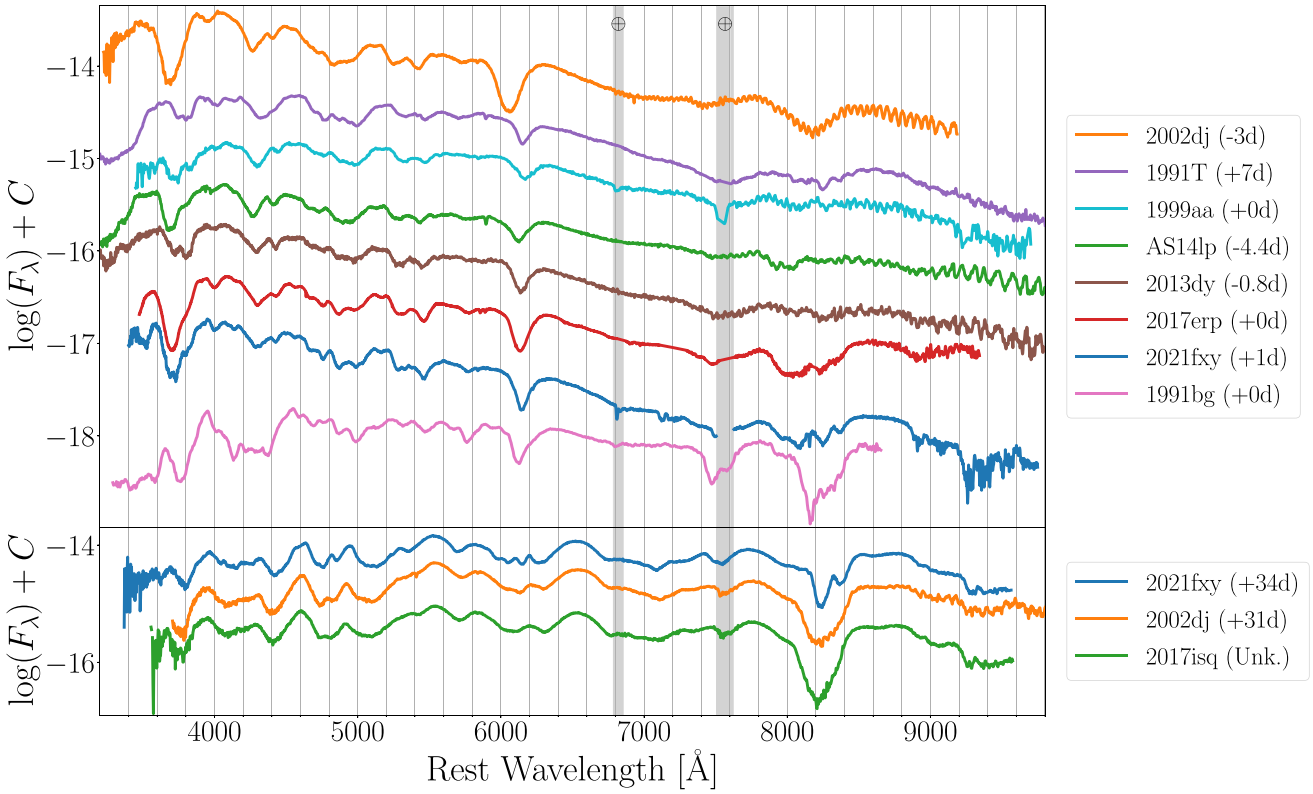

Figure 6. *Top Panel*: Comparison of SN 2021fxy near maximum light to its sibling SN 2002dj (BL), SN 2017erp (CN), SNe 1991T, 1999aa, 2013dy, and ASASSN-14lp (SS), and SN 1991bg (CL). *Bottom Panel*: Comparison of siblings SNe 2002dj and 2021fxy to potential sibling SN 2017isq roughly one month after maximum light.

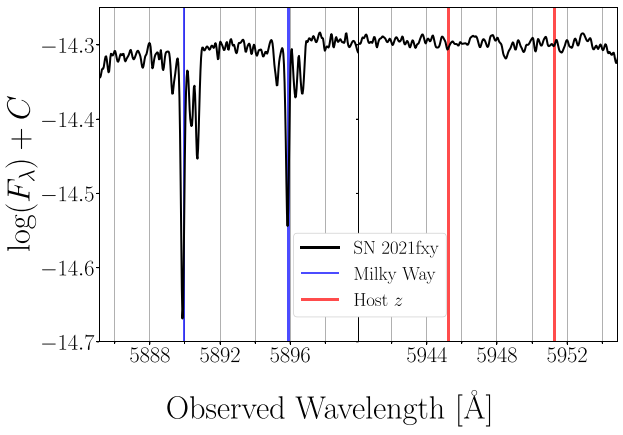

Figure 7. High-resolution spectrum of SN 2021fxy at +15.9 d focused on the narrow Na I D doublets. Four distinct sets of doublets are seen corresponding to interstellar clouds within the Milky Way (left). No detectable Na I D lines are seen at or near the host redshift of $z = 0.0094$.

This ensure that the smoothed errors encompass 68 per cent of the absolute value of the raw error spectrum. Measurements of the feature minima are then made by fitting the minimum value of the smoothed spectrum over a user-defined range. A Monte Carlo (MC) method is applied to generate a new instance of the smoothed spectrum and repeat this measurement 1000 times, with the overall error determined by adding the measurement error (as defined by the 1σ spread from the MC sample) to the error derived from the instrumental resolution (assumed to be 6 Å when not provided) in quadrature. As shown in Fig. 8, these measurements reveal that SN 2021fxy has similar velocities to other well-observed SNe Ia, including the extreme SS object SN 1991T (Filippenko et al. 1992; Jeffery et al. 1992; Phillips et al. 1992); SS objects like SNe 1999aa (Garavini et al. 2004; Silverman, Kong & Filippenko 2012) and 1999ee (Hamuy et al. 2002; Silverman et al. 2012); and CN objects including SNe 2011by (Stahl et al. 2020), 2011fe (Pereira et al. 2013; Stahl et al. 2020), and 2017erp (Brown et al. 2019). SN 2021fxy's sibling, SN 2002dj (an 2002bo-like or BL) is also shown for comparison (Pignata et al. 2008).

From the measurements in Fig. 8, we find that SN 2021fxy is a 'Normal' SN Ia within the Wang scheme, with $v_{\rm Si\,II} = 9900 \pm 250\,{\rm km\,s^{-1}}$ in the +1.3-d spectrum. SN 2021fxy belongs to the 'LVG' group in the Benetti scheme with a velocity gradient of $\dot{v} = -26 \pm 1\,{\rm km\,s^{-1}}$.

Using the Spextractor[11] and SNIaDCA[12] packages of Burrow et al. (2020), we measure the pEW's of the Si IIλ5972 and λ6355 features in the +1.3 d spectra to classify SN 2021fxy within the Branch scheme (Branch et al. 2006). As shown in Fig. 9, SN 2021fxy falls near the intersection of the 2σ confidence regions of the SS and CN groups, and has as a 64.1 per cent chance of belonging to the SS subgroup, compared to a 35.7 per cent chance of belonging to the CN subgroup. We note that some of the SNe Ia in the Burrow et al. (2020) sample located within a few Å of SN 2021fxy in the Branch diagram change

[11] https://github.com/anthonyburrow/spextractor
[12] https://github.com/anthonyburrow/SNIaDCA

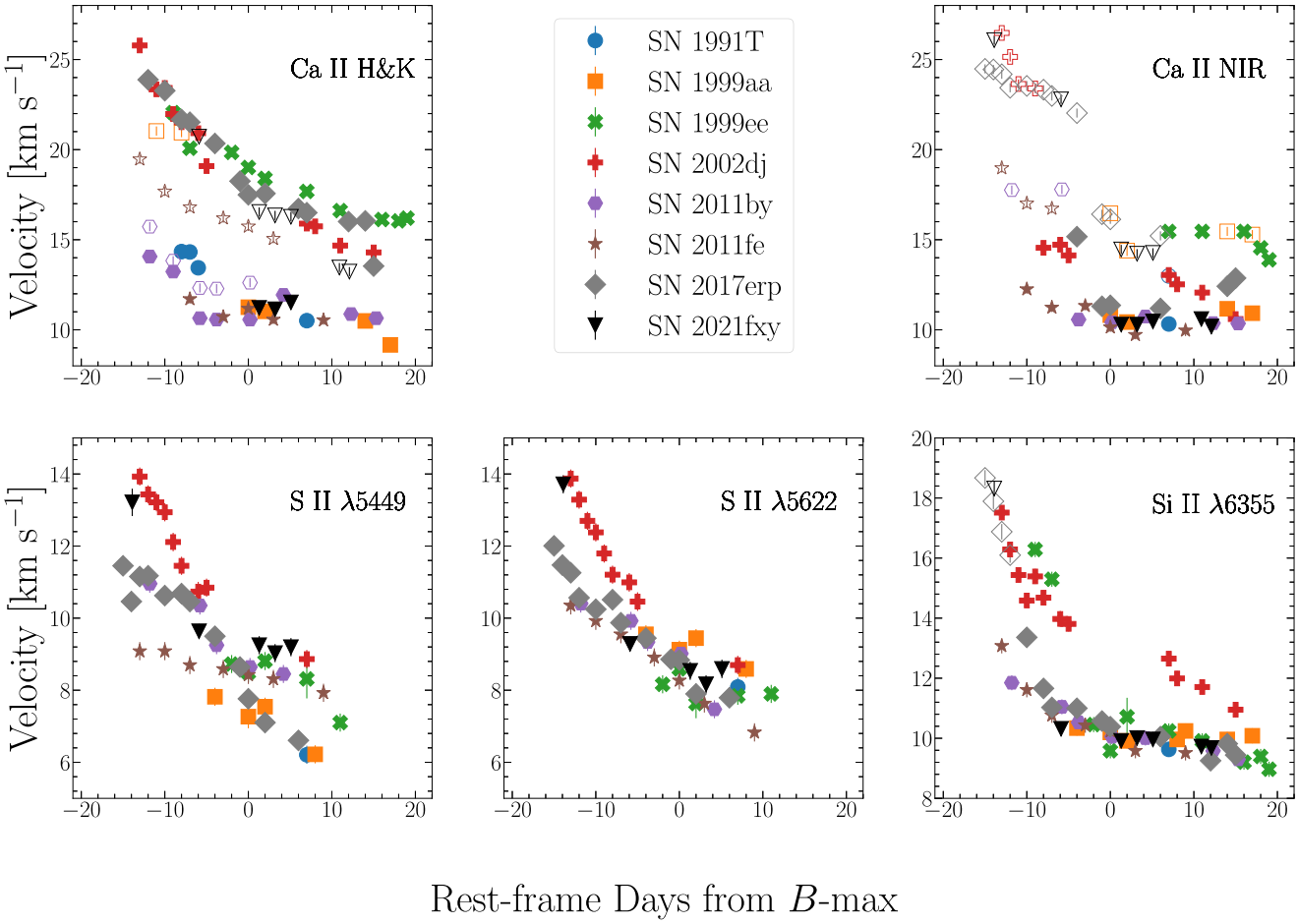

Figure 8. Velocities of prominent SNe Ia features during the photospheric phase. High-velocity components (when not blended with photospheric components) are noted with open symbols. In most cases, the error bars are smaller than the data markers.

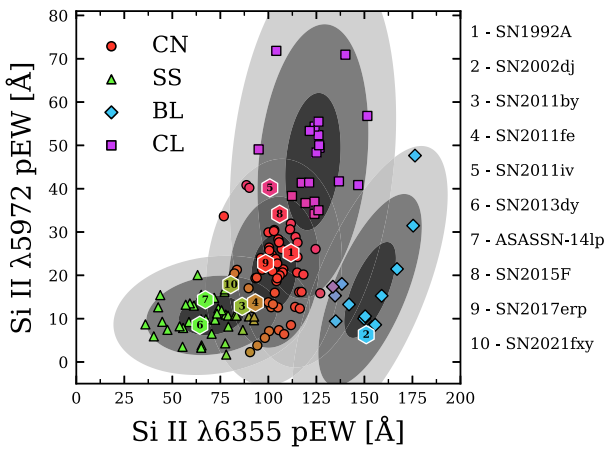

Figure 9. Branch diagram from Burrow et al. (2020) with SNe 2021fxy, 2002dj, and other members of the UV sample of spectroscopically normal SNe Ia overplotted. The colouring of each point corresponds to the likelihood of membership in a particular subgroup.

their group membership from CN to SS when additional information like the Si II velocity at max light and maximum B-band magnitude are included in the Gaussian Mixture Model which determines membership in the different Branch subgroups. Interestingly, SNe Ia such as SNe 2011by and 2011fe, which are typically associated with the core-normals also fall along the border of the CN and SS subgroups. While differences in the spectral epoch, methodology of measuring the pEW's and locations of the boundaries between the different subgroups may vary from diagram to diagram, it is clear that a significant number of 'normal' SNe Ia lie along the CN/SS border. While SN 1991T-like objects have been found to be an extreme subset of the SS group (Phillips et al. 2022), further study of the SNe Ia that reside along the CN/SS boundary of the Branch diagram may reveal information about the underlying physical differences between the two subgroups. Clearly, SNe 2011by, 2011fe, and 2021fxy are not SN 1991T-like objects, but rather belong to a group of objects that are near the middle of the SS/CN continuum.

3.2.2 UV spectra

The UV spectral sequence obtained with *HST*/STIS is shown in Fig. 10. The UV spectral features (identified in DerKacy et al. 2020) are relatively stable across the ∼10-d interval, with the most prominent evolution being the gradual weakening of the Cr II/Co II/Fe II blends near ∼2950 and ∼3200 Å.

Fig. 11 shows the maximum light UV spectrum of SN 2021fxy plotted against the spectra of other spectroscopically normal SNe Ia with *HST* UV spectra close to maximum light, including SNe 2011by (Foley & Kirshner 2013; Graham et al. 2015), 2011fe (Pereira et al.

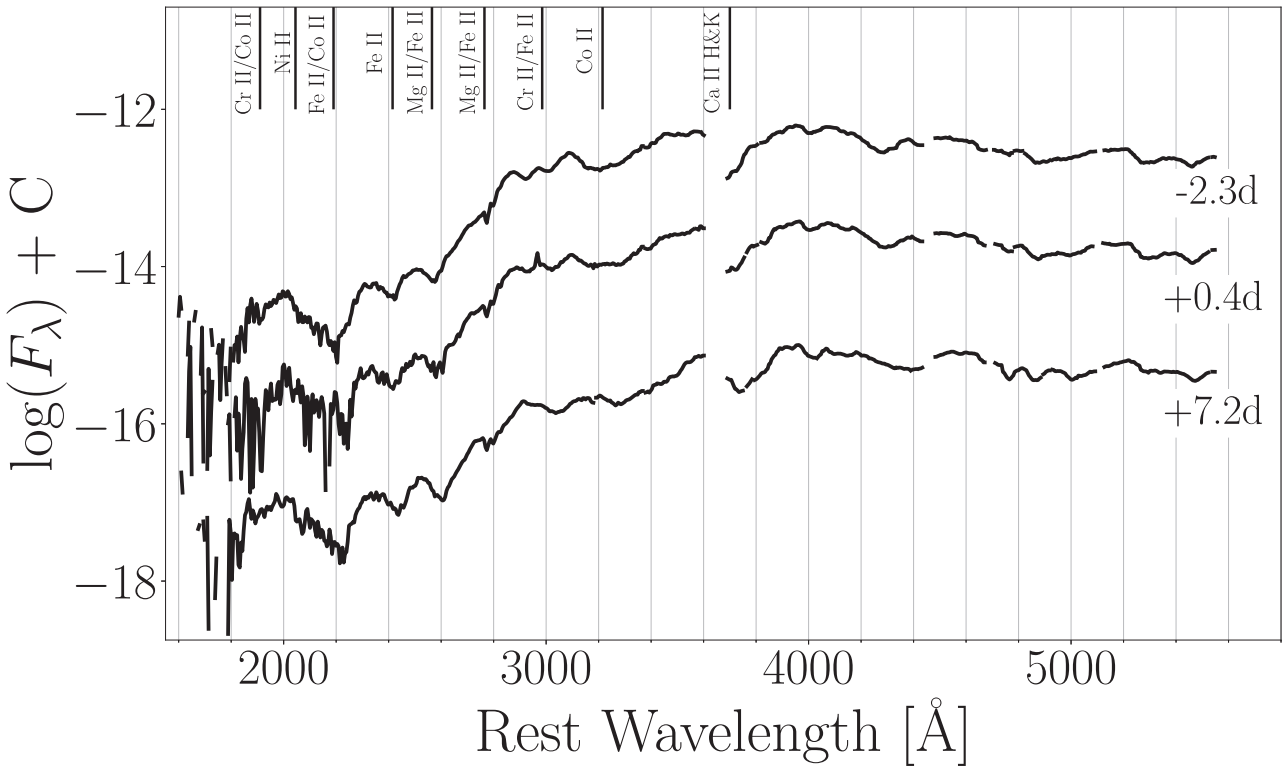

Figure 10. *HST*/STIS spectroscopy of SN 2021fxy corrected for Milky Way extinction. UV line identifications from the near-max models of DerKacy et al. (2020) are shown. Small gaps in the spectra result from the masking of bad pixels during the reduction.

2013; Mazzali et al. 2014), 2011iv (Foley et al. 2012; Gall et al. 2018), 2013dy (Pan et al. 2015), ASASSN-14lp (Foley et al. 2016; Shappee et al. 2016), 2015F (Foley et al. 2016; Burns et al. 2018), and 2017erp (Brown et al. 2019). From this comparison, we see that some SNe Ia show fluxes in the mid-UV which are suppressed relative to other objects in the sample. This 'MUV-suppression' can be quantified using the f_{2535} measure from Foley et al. (2016), defined as ten times the median flux from 2450 to 2620 Å relative to the peak flux of the spectrum. Across the sample, f_{2535} ranges from 0.405 (SN 2011iv) to 0.075 (SN 2017erp), with a mean value of 0.245 that evenly divides the sample into suppressed (SNe 2013dy, ASSASN-14lp, 2017erp, and 2021fxy) and non-suppressed (SNe 1992A, 2011by, 2011fe, 2011iv, and 2015F) objects. These four MUV-suppressed SNe also have mid-UV features which are blueshifted relative to their un-suppressed counterparts. Both the suppressed and 'un-suppressed' subsets show no common behaviors in either their near-UV spectral features or flux levels. However, the two subsets do show differences in their Ca II H&K features, with the suppressed SNe Ia possessing strong high velocity (HV) components that dominate the H&K feature. Unsuppressed SNe Ia show much weaker HV components and are dominated by the photospheric component. In the cases of the SNe Ia with *HST* spectra extending to the red half of the optical and NIR, those with MUV suppression (SN 2013dy and ASASSN-14lp) show higher flux levels than the unsuppressed SNe Ia, although it is unclear how much of these flux differences may be due to variations in host reddening. The source of this MUV suppression and its connection to feature locations and the Ca II H&K lines is explored further in Section 4.1.

3.2.3 *NIR spectra*

NIR spectra of SN 2021fxy are shown in Fig. 12. Compared to spectra of SN 2011fe at similar epochs (Hsiao et al. 2013), the +1.3 and +18.2-d spectra show broad similarities. Near maximum light, the Mg I and Mg II features between 0.9 and 1.1 μm appear significantly weaker in SN 2021fxy. A close examination of the C I λ1.0693 and Mg II λ1.0927 blend reveals that the feature is so weak that relative to the noise in the spectrum, we cannot conclusively identify the presence of either line. In the +18.2-d spectrum, high noise levels make identifications of many weak features difficult. The noise also complicates the measurement of the properties of the *H*-band break, $v_{\rm edge}$. Using the same procedure as Ashall et al. (2019a, b) we measure $v_{\rm edge} = 14\,100 \pm 100$ km s^{-1}, which is slightly higher than other measurements of $v_{\rm edge}$ at that epoch in the Ashall sample for SNe Ia with $s_{\rm BV} \gtrsim 1$, including SN 2011fe. We note that due to a bump in the spectra on the blueward side of the *H*-band break, an additional smoothing step using a 1D Gaussian kernel was required prior beginning the Guassian fit in order to achieve convergence. As a result, the reported error of $v_{\rm edge}$ accurately captures the statistical error associated with the fitting of the Gaussian center, but underestimates the total error. Furthermore, some SNe Ia in the CSP-II NIR spectral sample show blending on the blue side of the *H*-band break by an unidentified feature around +20 d, which complicates the fit (Hsiao et al. 2019; Ashall et al. 2019a, b). The emission peaks from Co II lines and blends of Iron Group Elements (IGEs) appear noticeably slower than those in 2011fe across all bands. By +38 d the spectra is dominated by IGE lines, similar to other NIR spectra at similar epochs in the sample of Marion et al. (2009).

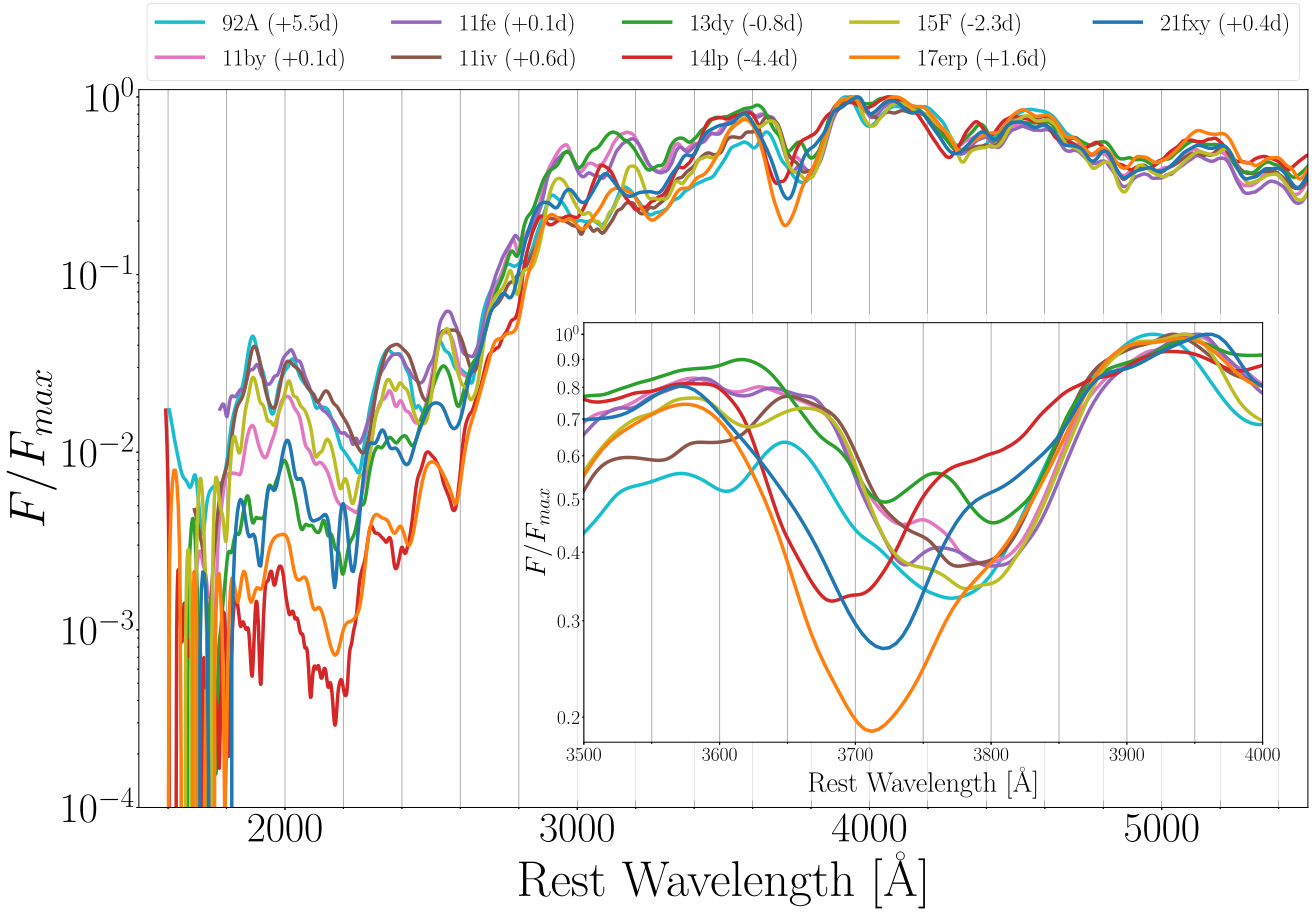

Figure 11. Comparison of SN 2021fxy with other spectroscopically normal SNe Ia having *HST*/STIS spectra, corrected for Milky Way extinction. Spectra are normalized relative to the maximum flux, which is located at either the Ca II H&K emission peak or the Si II blend emission peak at ∼4075 Å. Along with SNe 2013dy, ASASSN-14lp, and 2017erp, SN 2021fxy shows suppressed flux in the mid-UV and blue-shifted mid-UV features relative to SNe Ia without suppressed mid-UV fluxes. *Inset:* Close up of the Ca II H&K features, showing that SNe Ia with MUV flux suppression have strong HV Ca II H&K components which dominate the feature.

4 DISCUSSION

From Fig. 11, it is clear that MUV suppression is a common feature of SNe Ia; and that the strength of this suppression varies from object to object. However, explaining the root causes of these variations is difficult, as spectral formation in the ultraviolet is extremely complicated. Several physical factors, such as metallicity, density structure, and luminosity are known to have strong impacts on the observed spectra. All of these factors are inter-related, making the identification of which variable (or combination of variables) are responsible for the observed differences between SNe Ia quite difficult. Host reddening also becomes significant in the UV, as small differences in the estimate of the host R_V can significantly alter the observed flux levels. Therefore, rather than attempt to disentangle these related effects, we investigate the impact of these various factors, on-by-one, in order to determine how much of the observed MUV suppression they can explain.

4.1 Mid-UV suppression from host extinction?

One potential source of the mid-UV suppression in SNe Ia is the reddening of the SNe by dust in the host galaxy. However, estimating the amount of host extinction can be difficult, with different methods yielding significantly different results (see e.g. SN 2017erp in Brown et al. 2019). Additionally, numerous studies have shown that dust properties vary across different galaxies, and their extinction laws have different forms than that of the Milky Way (see e.g. Mathis 1990; Phillips et al. 2013, and references therein). Therefore, we attempt to correct for the host extinction using the published values of $E(B-V)_{\rm host}$ in combination with R_V values of ($R_V = 3.1$) and ($R_V = 2.1$), representing hosts with Milky Way-like extinction and low-metallicity hosts like the Small Magellanic Cloud (SMC; Gordon et al. 2014; Yanchulova Merica-Jones et al. 2021), respectively. We also use the supernovae light curves to attempt to fit the value of R_V in the host galaxy using `SNooPy`'s `colour_model`, which simultaneously fits both $E(B-V)_{\rm host}$ and R_V based on the intrinsic SN Ia colours determined by Burns et al. (2014). Since both parameters appear within the same fitting term; they are covariant; and in cases where the total host extinction is small, the fit can become insensitive to the value of R_V. If this occurs, we impose a prior derived from a Gaussian Mixture Model representing the distribution of R_V as determined from the CSP-I sample in Burns et al. (2014), and the data is refit using a Markov Chain Monte Carlo (MCMC) method. The results of these fits are shown in Table 3. UV spectra corrected for this host extinction with the fitted values of R_V and $E(B-V)$ are shown in Fig. 13.

No matter which value of R_V is chosen to correct for host extinction, a subset of our objects still show significant MUV

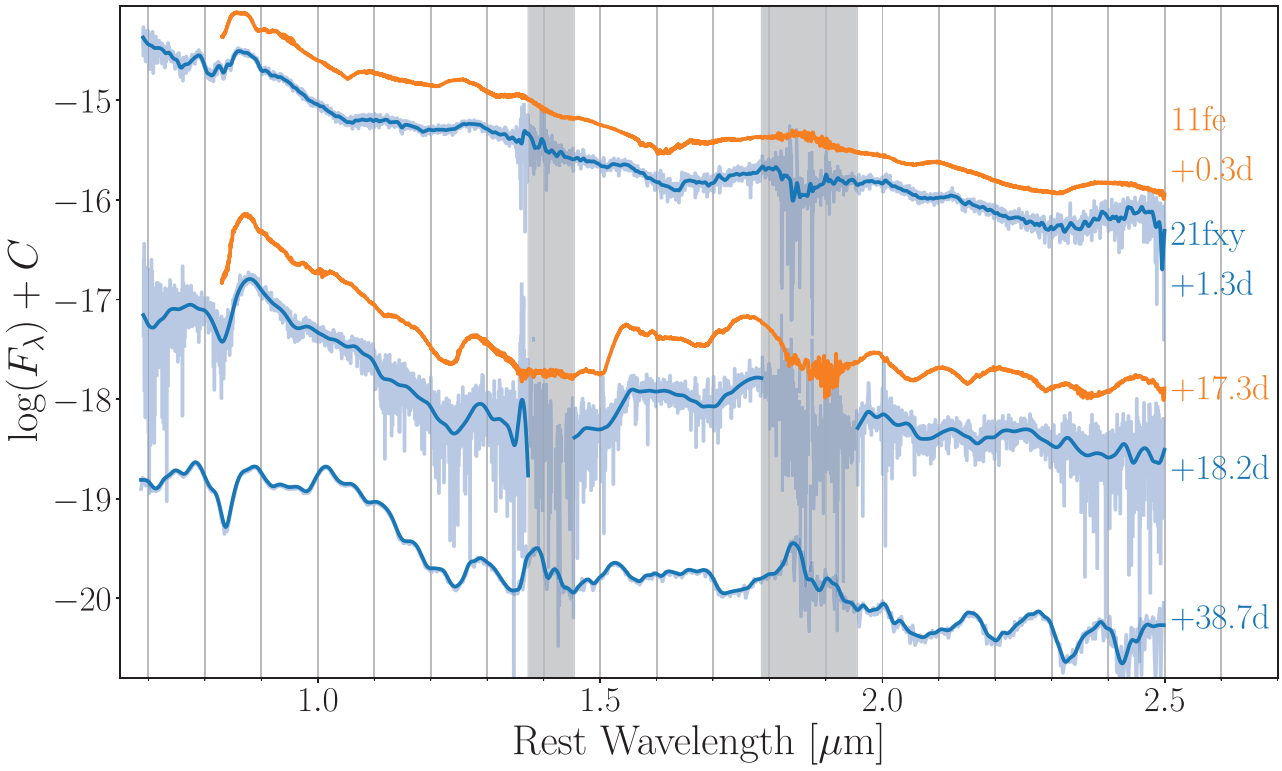

Figure 12. NIR spectra of SN 2021fxy. NIR spectra of SN 2011fe from Hsiao et al. (2013) at similar epochs are shown for comparison. Smoothed spectra are plotted in the foreground, with the raw spectra shown behind. The epoch relative to rest-frame *B*-band maximum is noted next to each spectrum. Grey boxes mark regions of strong telluric absorption. The noisy telluric regions between the NIR bands in the +18.2 d smoothed spectrum are removed for clarity.

suppression. Corrections for host extinction do, however, reduce the spread in relative flux between SNe showing MUV suppression. After correcting for host extinction, SN 2013dy no longer shows significant MUV flux suppression, instead showing relative fluxes consistent with unsuppressed SNe Ia. However, SN 2013dy was one of multiple SNe (along with SNe 2011fe, 2011iv, and 2021fxy) with SNooPy fits that were initially insensitive to the value of R_V, but was the only one of this group where the MCMC fitting resulted in significant host extinction. All SNe that required MCMC fits show no evidence of significant host extinction from spectral observations. Therefore, it is likely that the values derived by SNooPy represent overestimates of the host extinction for these four SNe.

Table 3. Host extinction fitting with SNooPy.

Object	$E(B-V)_{\rm host}$ (mag)	R_V
2011by	0.19 ± 0.06	3.17 ± 0.52
2011fe[a]	0.08 ± 0.06	3.10 ± 0.16
2011iv[a]	−0.02 ± 0.06	3.11 ± 0.06
2013dy[a]	0.23 ± 0.06	3.10 ± 0.23
ASASSN-14lp	0.34 ± 0.06	2.27 ± 0.17
2015F	0.15 ± 0.06	4.09 ± 0.31
2017erp	0.18 ± 0.06	2.80 ± 0.51
2021fxy[a]	0.05 ± 0.06	3.11 ± 0.05

[a]Objects for which the initial fit was insensitive to R_V.

4.2 Common properties of MUV-suppressed SNe Ia

With host extinction unable to explain the observed MUV suppression for those objects showing significantly suppressed MUV fluxes, we now turn our focus to identifying physical explanations for this behaviour based on commonalities in the observational properties of the SNe in our UV sample. Examining the SNe Ia showing evidence of MUV suppression, there are a few commonalities shared by all four objects that are readily apparent.

As noted in Section 3.2, those SNe Ia with MUV flux suppression also have feature minima in the mid-UV which are bluer relative to SNe Ia lacking MUV flux suppression. The relationship between the location of the flux minima for three mid-UV features (the Ni II/Fe II/Co II blend between 2000–2400 Å, the Fe II feature between 2350 and 2550 Å, and the Fe II/Mg II blend between 2500 and 2700 Å) and the relative flux at those minima are shown in Fig. 14. The relationship is strongest in the Fe II/Mg II blend, but is strong across all three features. Similarly, the correlations are strongest when the spectra are corrected only for MW extinction, as shown in Fig. 13, but the effect persists for all variations of host extinction corrections. This effect arises naturally, as the opacity in the mid-UV originates primarily from the line blanketing of iron group elements (DerKacy et al. 2020), which increase the effective opacity in the mid-UV as their velocity increases (Wang et al. 2012).

As shown in Hauschildt (1992) the equation of radiative transfer (RTE) can be written in the co-moving frame as:

$$a_r \frac{\partial I_\lambda}{\partial r} + a_\mu \frac{\partial I_\lambda}{\partial \mu} + a_\lambda \frac{\partial \lambda I_\lambda}{\partial \lambda} + 4 a_\lambda I_\lambda = \eta_\lambda - \chi_\lambda I_\lambda \quad (1)$$

where the symbols have their usual meanings and the a's are defined in equation (3) of Hauschildt (1992). This form of the RTE leads to an effective opacity $\hat{\chi} \equiv \chi + a_\lambda(4 + \frac{\lambda_l}{\lambda_l - \lambda_{l-1}})$, where the λ_l represents the l-th element in the wavelength grid and the term comes from

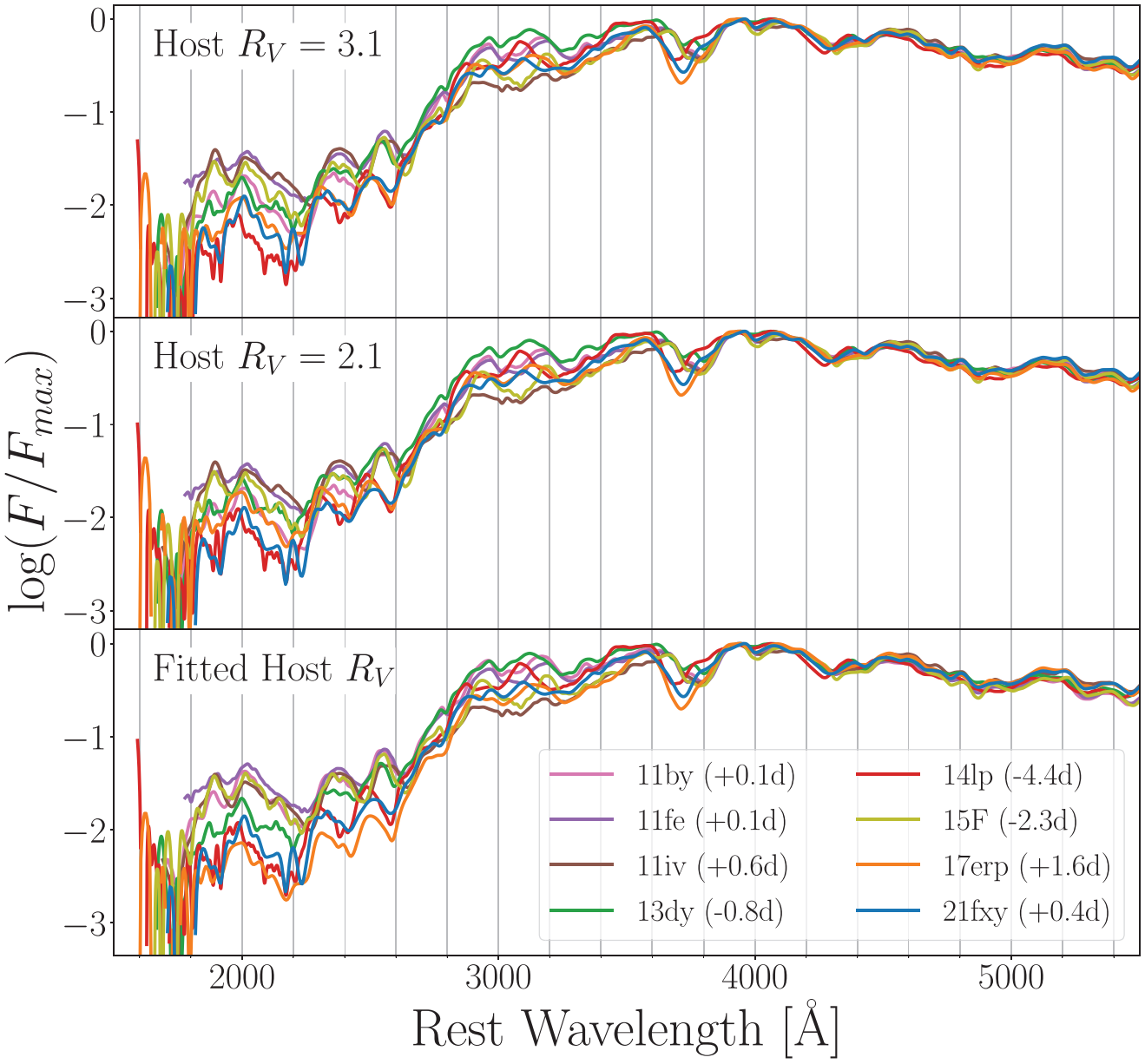

Figure 13. Same as Fig. 11, but corrected for host extinction assuming $R_V = 3.1$ (top), $R_V = 2.1$ (middle), and the fitted R_V (bottom). SN 1992A is omitted due to insufficient photometry necessary for robust estimations of $E(B-V)_{\rm host}$ and R_V.

finite differencing the $\frac{\partial}{\partial\lambda}$ term. This effective opacity $\hat{\chi}$, leads to increased opacity at high velocity, which is particularly enhanced by line-blanketing in the UV by IGEs.

Further support for the presence of high velocity material in MUV-suppressed SNe Ia is found in the obvious dominance of the HV component of the Ca II H&K lines over the photospheric components in their spectra. We can quantify this dominance using the $R_{\rm HVF}$ measure established by Childress et al. (2014), originally defined for the Ca II NIR triplet but now redefined here for the H&K lines as

$$R_{\rm HVF} = \frac{pEW({\rm HVF_{H\&K}})}{pEW({\rm PVF_{H\&K}})}. \quad (2)$$

To determine the value of $R_{\rm HVF}$, we again turn to the `misfits` package. After the *HST* spectra are smoothed as described in Section 3.2, the Ca H&K features are fit with multiple Gaussian components using the `width.gaussians` option. The number of Gaussians is chosen by the user, and compared to the number of components required to recreate the Ca NIR triplet to avoid overfitting. These Gaussians are integrated with respect to a pseudo-continuum derived from user-defined continuum regions on either side of the H&K feature to determine the pEW of both the photospheric (PVF) and high velocity (HVF) features. As before, an MC method is then used to generate 1000 new instances of the smoothed spectrum and the measurements repeated. The values of the pEW's and the statistical uncertainties derived from the MC method are reported in Table 4. While the reported errors likely underestimate the true error, the Ca H&K lines are located near the peak of the SED (where S/N should be highest) in the near-max light *HST* observations. Therefore, the reported errors are not completely unreasonable.

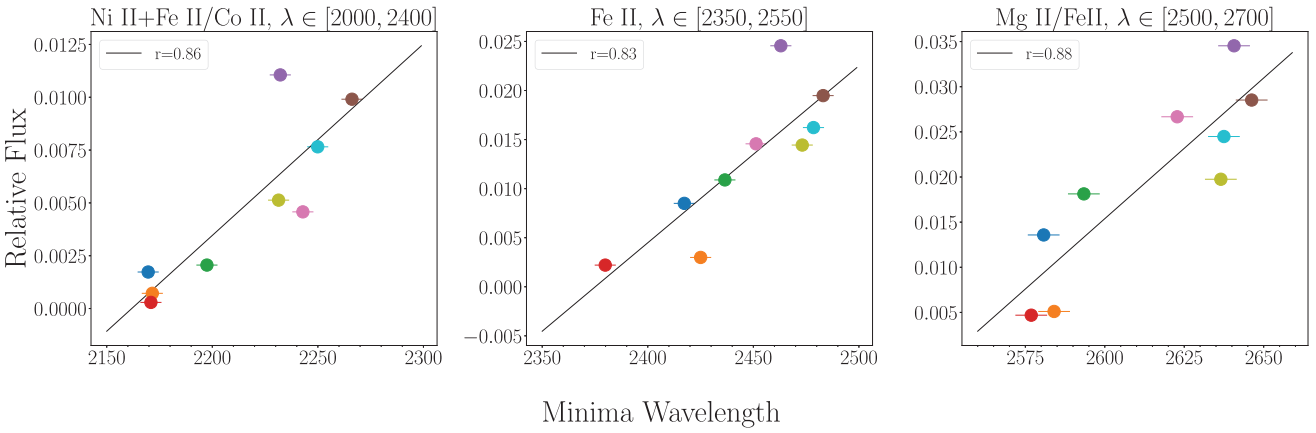

Figure 14. The relative flux ($F/F_{\rm max}$) versus minimum wavelength for three MUV features, with the best-fitting linear regression and Pearson correlation coefficient r, also shown. For all data points, the relative flux error bars are smaller than the markers. The spectra were corrected for Milky Way extinction, but not host extinction. Data points share the same colouring as Fig. 11.

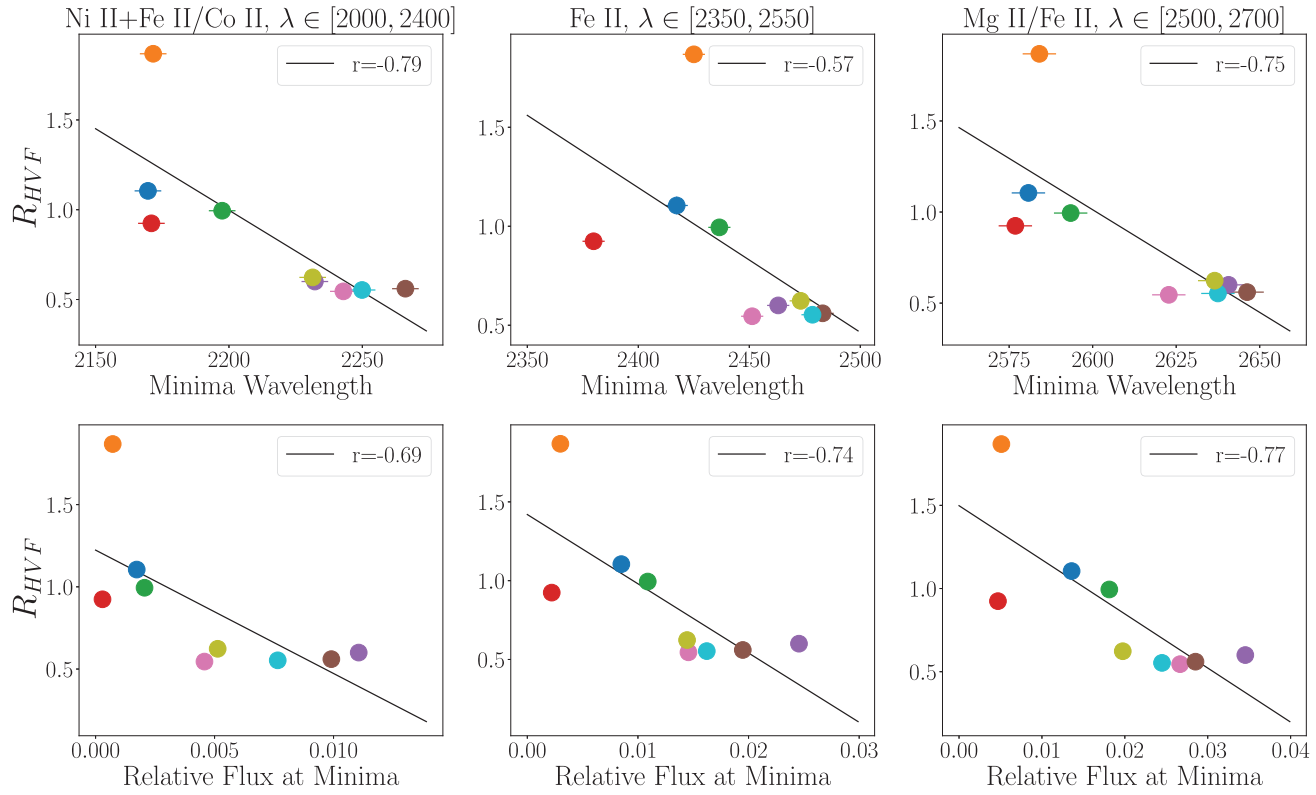

Figure 15. *Top row*: $R_{\rm HVF}$ versus minimum wavelength for three MUV features. The best-fitting linear regression and the Pearson correlation coefficient r, are also shown. *Bottom row*: $R_{\rm HVF}$ versus relative flux ($F/F_{\rm max}$) at the minimum wavelength for the same MUV features. In all panels, the errors in $R_{\rm HVF}$ are smaller than the markers, while in the bottom panels the relative flux error bars are smaller than the markers. As in Fig. 14 spectra corrected for Milky Way extinction, but not host-galaxy extinction. Data points share the same colouring as Fig. 11.

We find that MUV-suppressed SNe have values of $R_{\rm HVF} \gtrsim 0.9$, while non-suppressed SNe have $R_{\rm HVF} \lesssim 0.6$. $R_{\rm HVF}$ correlates with both the minimum wavelength and the relative flux at those minima for the three features specified in Section 4.1, although whether it correlates more strongly with the minimum wavelength or the relative flux is feature dependent, as seen in Fig. 15. As before, the correlations are present in all three features, although the correlation between $R_{\rm HVF}$ and the minimum wavelength of the Fe II blend is noticeably weaker than those of the other two MUV features. Again, these correlations persist after correcting for host extinction.

Other effects may also play a role in producing MUV flux suppression coupled with a blue-shift in MUV features, including changes in density structure or progenitor metallicity. This same blue-shift in the mid-UV features was achieved by Barna et al. (2021) in their modelling of ASASSN-14lp by using a modified, shallower version of the W7 density profile. Because both shallower

Table 4. pEW measurements.

Object	HVF pEW (Å)	PVF pEW (Å)	R_{HVF}
1992A	26.96 ± 0.95	48.75 ± 0.62	0.55 ± 0.02
2011by	26.43 ± 0.24	48.46 ± 0.25	0.55 ± 0.01
2011fe	29.29 ± 0.01	48.81 ± 0.01	0.60 ± 0.01
2011iv	23.88 ± 0.26	42.62 ± 0.24	0.56 ± 0.01
2013dy	37.18 ± 0.26	37.39 ± 0.26	0.99 ± 0.01
ASASSN-14lp	58.06 ± 0.14	62.83 ± 0.50	0.92 ± 0.01
2015F	26.38 ± 0.32	42.33 ± 0.29	0.62 ± 0.01
2017erp	66.95 ± 0.52	35.83 ± 0.51	1.87 ± 0.03
2021fxy	68.78 ± 2.36	62.25 ± 1.36	1.10 ± 0.04

Note. The reported errors only include the statistical uncertainties derived from the MC fitting of the pEW's.

density profiles (e.g. changes in the relative distribution of a constant mass in the outer layers) and higher line velocities (e.g. additional material extending the line-forming regions within a fixed density profile) produce broader lines, it is difficult to distinguish between the two effects as the primary source of the flux suppression from RTE alone. As the amount of metals in the outer ejecta increases, so does the strength of the line blanketing; resulting in the photosphere being located at higher velocities, and thus suppressing flux in the MUV. However, large changes in metallicity cannot be responsible for this suppression, as they induce other changes in the broader UV spectrum that are not seen in the observed spectra (see Section 4.3 for more details, see also Lentz et al. 2000; Barna et al. 2021). DerKacy et al. (2020) also found that their lower luminosity models produced these same MUV features blueshifted relative to their higher luminosity models; primarily due to temperature variations in the outer portions of the ejecta altering the ionization balance between Fe II and Fe III significantly enough to change the relative composition of the line blends that comprise these MUV features. If the MUV suppression is due to higher velocities exhibited in observed spectral features, one would expect that BL or High-Velocity SNe Ia in general would exhibit a strong MUV suppression.

Turning our attention to properties beyond those in the UV spectra, in Fig. 11, we see that in the mid-UV, SNe 2013dy and 2021fxy have similar flux values and feature locations. The same is true of ASASSN-14lp and SN 2017erp. However, in the near-UV, SN 2013dy more closely resembles the spectra of SNe 2011fe and 2011iv. Meanwhile, ASASSN-14lp and SN 2021fxy have nearly identical spectra between 3000 and 3600 Å, with SN 2017erp showing lower NUV fluxes than any other SN Ia with significant MUV suppression. Returning to Fig. 4, all four SNe are members of the NUV-red group, following the same general evolutionary track, albeit with significant scatter. ASASSN-14lp and SN 2017erp generally appear redder than SNe 2013dy and 2021fxy at all epochs.

The bigger picture becomes even less clear when we begin to consider the optical spectral properties of the MUV-suppressed SNe. SNe 2013dy, ASASSN-14lp, and 2021fxy are all members of the SS class, while SN 2017erp belongs to the CN class. While the spectral behaviour of SNe 2013dy and ASASSN-14lp are typical of members of the SS subgroup, SNe 2017erp and 2021fxy share many characteristics, including nearly identical optical spectra and light curve parameters, ($s_{BV,\,21fxy} = 0.99 \pm 0.03$, $\Delta m_{15}(B)_{21fxy} = 1.05 \pm 0.06$; $s_{BV,\,17erp} = 0.99 \pm 0.03$, $\Delta m_{15}(B)_{17erp} = 1.05 \pm 0.06$). When we expand this comparison to include spectra both before and after maximum light, we find that both object's spectra show similar feature velocities, line profiles, and line strengths for nearly all of their lines throughout their evolution. The notable exceptions to this being the Si II λ5972 and λ6355 lines. While it is tempting to establish a familial relationship between 2021fxy and 2017erp, given the numerous similarities is their spectral and photometric properties, unlike the 'twin' supernovae 2011by and 2011fe, SNe 2017erp and 2021fxy are not members of the same Branch group (see again Fig. 9, also Section B); nor are they 'siblings' hosted in the same galaxy. SNe 2021fxy and 2017erp also show significantly different continuum levels in the optical, as seen in Fig. 16, which persists throughout the photospheric phase. Despite these differences, from the *HST* spectra, SNe 2021fxy and 2017erp produce a flux ratio bluewards of ∼5600 Å that is comparable to the one between SNe 2011by and 2011fe at maximum light, as seen in the lower panel of Fig. 16. As such, we analyse the *HST* spectra of SNe 2017erp and 2021fxy in an attempt to determine the source of their UV flux differences.

4.3 Comparing SNe 2017erp and 2021fxy

4.3.1 Optical spectra similarities

Early on, both supernovae show similar high-velocity (HV) Si II lines with the velocity of the feature in SN 2017erp declining from −21 600 km s^{-1} to −18 000 km s^{-1} from the first spectrum taken at −17.0 d to the one taken at −14.1 d. The first spectrum of SN 2021fxy at −13.9 d shows HV Si II at −18 200 km s^{-1} (see Fig. 17). Roughly a week later, the HV Si II has mostly faded from both supernovae. However, the −5.9-d spectrum of SN 2021fxy shows a flat-topped emission peak associated with a feature detached from the underlying photosphere; compared to the traditional P-Cygni profile seen in the −8.5-d spectrum of SN 2017erp, where the feature begins forming at the photosphere (see Section B for further details). In SN 2021fxy, the Si II remains detached throughout the photospheric phase, until it begins to be polluted by Fe lines, which first appear around +11/+12 d, and are clearly present at +15.7 d. In contrast, the Si II feature in SN 2017erp does not detach from the photosphere until +6 d, and does not begin to show signs of the photosphere entering the Fe-rich inner region until +17 d. Taken together, these differences support the classification of SN 2021fxy as a SS object. Nugent et al. (1995) showed that the Branch sequence (neglecting BL) is driven by differences in temperature, with CL being coolest and SS being hottest. To zeroth order these temperature differences may be associated with the total amount of ^{56}Ni produced in the explosion. Thus, in a near Chandrasekhar mass progenitor scenario we expect SS to produce somewhat more ^{56}Ni and somewhat less silicon, leading to more rapid evolution in the Si II features for SS as compared with CN supernovae.

4.3.2 UV flux differences

Due to the complicated relationships between physical factors (metallicity, density structure, and luminosity) that have strong impacts on UV spectral formation, attributing UV spectral variations to an individual factor is difficult. Therefore, we examine the flux ratios from self-consistent sets of models, varying one factor at a time, to place limits on the relative differences in metallicity and luminosity between SNe 2017erp and 2021fxy by assuming the observed UV differences are caused solely by an individual factor. Proper treatment of differences in density structure require the construction of detailed abundance distributions of each SN under consideration and are therefore left to future work.

4.3.2.1 Metallicity variations – Using the $t = 15$-d models of Lentz et al. (2000), we can explore differences in the relative progenitor

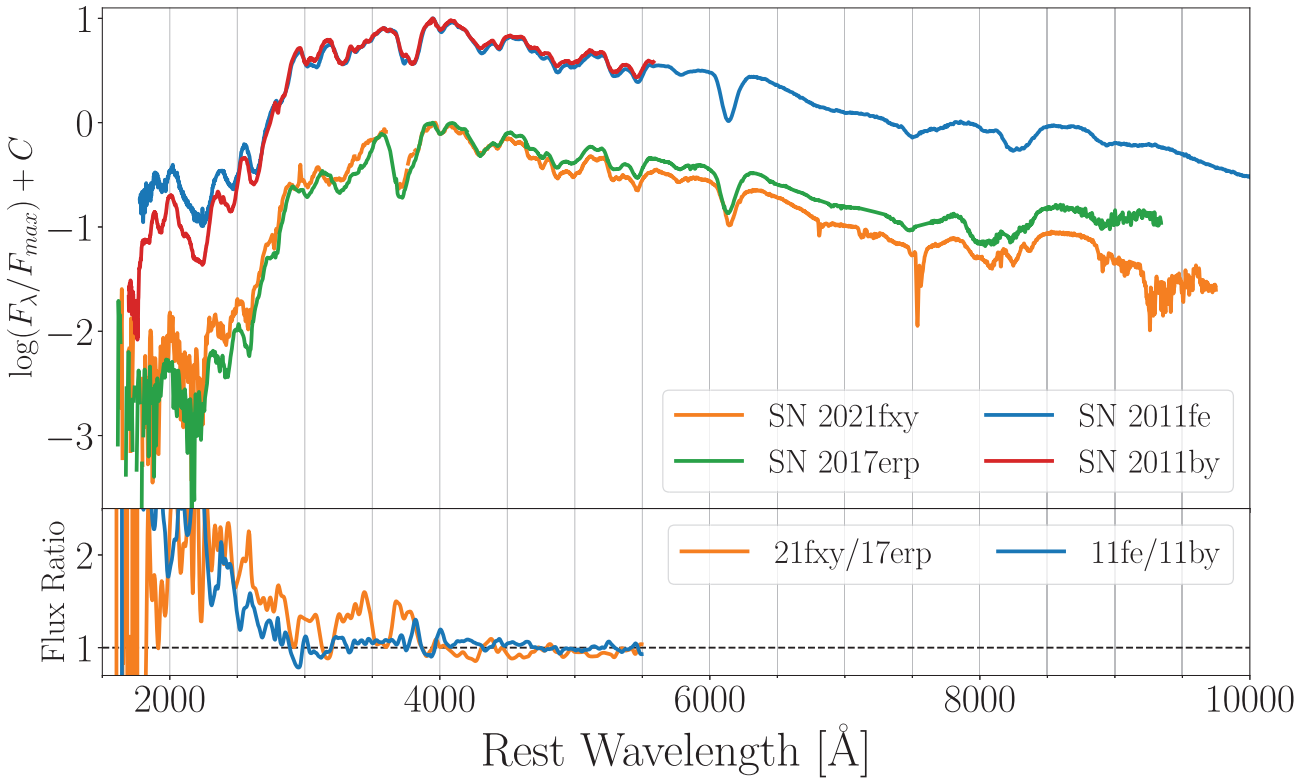

Figure 16. *Top panel*: Combined UV/Optical spectra of SN 2021fxy and 2017erp at maximum light compared to those of SN 2011fe and 2011by. *Bottom panel*: Flux ratio of SN 2021fxy/2017erp compared to that of SN 2011fe/2011by, as determined from the *HST* portions of the spectra.

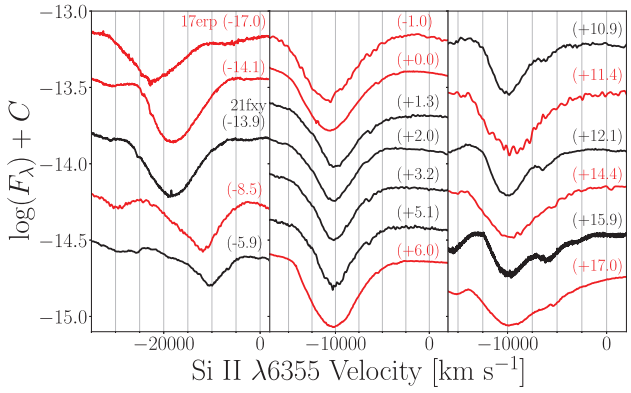

Figure 17. Comparison of Si II λ6355 line evolution in SN 2021fxy and SN 2017erp.

metallicity as the source of the UV differences between the two supernovae. These models are NLTE simulations based on W7, with the abundances of all elements heavier than oxygen in the unburned C + O layer ($v \gtrsim 15\,000$ km s^{-1}) scaled by factors of ζ = 1/30, 1/10, 1/3, 3, and 10 relative to solar metallicity. As previously noted by Foley & Kirshner (2013), the flux ratios from models with the same metallicity ratio produce the same general trend across the UV, and therefore are only able to infer relative metallicities between the two SNe, not differentiate the absolute metallicities of the supernovae. In exploring the impact of relative metallicity differences between SNe 2021fxy and 2017erp, we examine only the region between 2000 and 2500 Å, as spectral formation in this region is almost entirely determined by iron group elements (see fig. 8 of DerKacy et al. 2020). No combination of any two Lentz models is able to reproduce the flux ratio of 2021fxy/2017erp across the entire wavelength range, in part due to the diminishing ability of these models to distinguish between increasingly large differences in the relative metallicity. The best match to the 2021fxy/2017erp flux ratio is produced by the $\zeta_{1/30}/\zeta_{10}$ curve ($\chi^2 = 166.87$, $\chi^2_\nu = 1.7$). If we instead fit over the entire *HST* spectra with $\lambda > 1800$ Å, we find that we can no longer distinguish between the flux ratio curves produced by the 1/300 ($\chi^2 = 328.19$), 1/100 ($\chi^2 = 328.23$), and 1/90 ($\chi^2 = 341.10$) metallicity ratios. This result matches what we see in the top panel of Fig. 18, as each of these three curves are virtually indistinguishable redward of 2500 Å, and only distinguished by small variations in the height of a few peaks between 2000 and 2500 Å where metallicity differences should be most apparent.

4.3.2.2 Luminosity variations – The bottom panel of Fig. 18 shows selected flux ratios of models from DerKacy et al. (2020) compared to the flux ratio of 2021fxy/2017erp. Analysis of these models reveal that unlike the flux ratios generated from the models of Lentz et al. (2000), the flux ratios generated from the DerKacy et al. (2020) models are sensitive to both the relative luminosity difference and absolute luminosity of the model. This is due to the luminosity differences inducing temperature variations in the outer ejecta that alter the shape of the underlying continuum, as well as the excitation and ionization states of the outer ejecta. The differences produce different strengths and locations of spectral features in the ejecta, resulting in unique flux ratio curves dependent on the luminosities of the two spectra in the

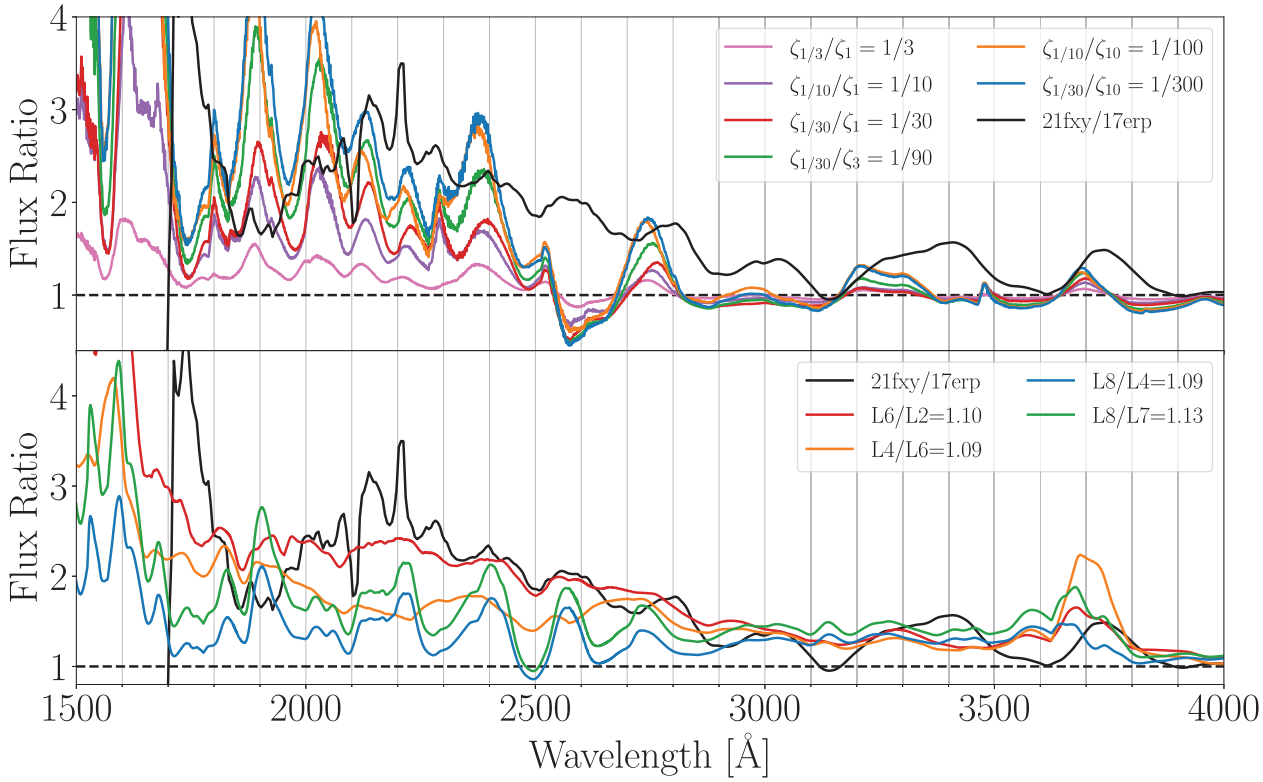

Figure 18. *Top panel*: Flux ratios of the Day 15 spectral models from Lentz et al. (2000) with the flux ratio of SN 2021fxy to SN 2017erp overplotted. *Bottom panel*: Flux ratios for selected models of DerKacy et al. (2020) compared to the flux ratio of SN 2021fxy to SN 2017erp.

ratio. In effect this is an application of the Spectral-fitting Expanding Atmosphere Method (SEAM; Mitchell et al. 2002; Baron et al. 2004; Dessart & Hillier 2010). We find good agreement between the flux ratios produced from the L6/L2 models ($\chi^2 = 190.77$, $\chi^2_\nu = 0.25$) and the flux ratio of 2021fxy/2017erp, implying that SN 2021fxy has a peak bolometric luminosity 10 per cent higher than that of SN 2017erp.

However, we caution against too strong an interpretation of these results as the model and input luminosities used in DerKacy et al. (2020) were only simulated at one epoch and were chosen because they best reproduce SN 2011fe, which is known to have the bluest UV minus optical colours among SNe Ia with UV spectra (Brown et al. 2017; Brown et al., in preparation). Furthermore, both the best-fitting luminosity and metallicity ratio curves only broadly capture the observed differences between SNe 2017erp and 2021fxy in the mid-UV, where the differences in both properties are expected to be the greatest. It is only when the differences in flux from the remainder of the UV and optical are examined (see again Fig. 16), we find that the behaviour is more consistent with those expected from differences in luminosity than metallicity (Lentz et al. 2000; DerKacy et al. 2020). In the case of SNe 2011by and 2011fe, Graham et al. (2015) found that the inclusion of additional information, such as UV time series spectra and nebular spectra, may disfavour certain explanations like metallicity differences as the root cause of UV variations; despite the inability of any single parameter to adequately reproduce the observed UV differences without inducing unobserved differences in the optical. Foley et al. (2020) also showed that there are significant differences in the luminosities of SNe 2011by and 2011fe after re-calibrating the distance to NGC 3972 (host of SN 2011by) which may be explained by multiple mechanisms. Additional work to verify the relationship between UV spectra and SNe Ia properties like metallicity and luminosity across more models and epochs in a self-consistent manner is currently underway.

Table 5. Comparison of light-curve parameters.

Parameter	SN 2021fxy	SN 2002dj
t_{max} (MJD)	59 305.1 ± 0.3	52 450.9 ± 0.4
s_{BV}	0.99 ± 0.04	0.94 ± 0.04
$E(B-V)_{host}$ (mag)	0.02 ± 0.06	0.10 ± 0.06
μ (mag)	32.87 ± 0.09	32.97 ± 0.09

4.4 Sibling's analysis

Detailed analyses of SNe Ia siblings (e.g. two or more SNe Ia hosted in the same galaxy) allow us to test many of our assumptions about SNe Ia as cosmological distance indicators. By virtue of sharing the same host, many of the factors that increase the scatter in cosmological distance measurements are eliminated, including dependencies on properties of the host galaxy such as host mass and metallicity, and peculiar velocities (Sullivan et al. 2010; Brown 2014; Burns et al. 2020; Scolnic et al. 2020; Hoogendam et al. 2022).

The one confirmed sibling to SN 2021fxy, SN 2002dj, was studied in depth by Pignata et al. (2008), and determined to be a Ia-BL within the Branch scheme with several similarities to SN 2002bo. Using `SNooPy`, we fit the photometry of SN 2002dj, with the results compared to those of SN 2021fxy in Table 5. From the results, we find that the implied distance modulus to NGC 5018 agree to 1.2σ,

within the average $\Delta\mu$ of other sibling SNe Ia studied by Burns et al. (2020). Both values are also consistent with the redshift derived value to less than 1σ. The inferred host extinctions are consistent at the 1.3σ level. The different estimates of $E(B-V)$ are likely due to different local environments in the vicinity of the two SNe. SN 2002dj was found to be coincident with an extended emission region appearing as a warped disc covering portions of NGC 5018, and is associated with regions of star formation (Goudfrooij et al. 1994; Pignata et al. 2008). SN 2021fxy exploded in a part of NGC 5018 unassociated with this emission region.

5 CONCLUSIONS

We present detailed photometric and spectroscopic follow-up of SN 2021fxy, a SN Ia discovered in NGC 5018 for which we also obtained UV photometry with *Swift/UVOT* and UV spectroscopy with *HST*/STIS. Ground-based photometric and spectroscopic observations were obtained as part of the Precision Observations of Infant Supernova Explosions (POISE; Burns et al. 2021), the Aarhus-Barcelona FLOWS, and NUTS2 collaborations. Our observations reveal that SN 2021fxy has a normal light curve consistent with a normal-bright SN Ia. The $B-V$ colours of SN 2021fxy are red in the first days after explosion but rapidly evolve blueward. Optical spectra show SN 2021fxy to be a member of the SS group, located near the border of the CN and SS groups within the Branch diagram. In contrast to other SS objects from the Stritzinger et al. (2018) sample, SN 2021fxy is the only known SS object to show an early-time red $B-V$ colour, suggesting that early colour diversity a complex phenomenon not captured in SN Ia sub-classification schemes. A better understanding of the diversity of early-time colours and their connections to observational properties, progenitor systems, and explosion mechanisms are a key scientific goal of the POISE collaboration.

UV spectra show that when compared to other spectroscopically normal SNe Ia, SN 2021fxy is a member of a group of objects with flux suppression in the mid-UV, which cannot be explained by host reddening alone. Objects with MUV flux suppression all belong to the NUV-red group of SNe Ia, possess MUV features that are bluer than their non-suppressed counterparts and HV components in their Ca II H&K lines that are dominant over the photospheric components, as measured by the quantity $R_{\rm HVF}$. One potential cause of this suppression is an increased effective opacity in the mid-UV from IGEs at higher velocities, which would imply a continuous distribution of MUV flux values in SNe Ia. However, the presence of the HV Ca features could indicate that shells of material within the ejecta are responsible for the additional line blanketing. In either case, more UV spectral observations of SNe Ia are needed, especially of BL or high-velocity supernovae, in order to determine the physical mechanism responsible for the MUV flux suppression.

Among those SNe Ia with MUV flux suppression, SNe 2021fxy and 2017erp show remarkable similarities despite belonging to the SS and CN Branch subgroups, respectively, which allow us to probe the mechanisms responsible for variations between different MUV-suppressed objects. We find that the flux differences between SNe 2021fxy and 2017erp in the UV are comparable in size to those between SNe 2011by and 2011fe, but are instead likely due to variations in the intrinsic luminosity differences between the two SNe; not metallicity differences as has been suggested for SNe 2011by and 2011fe. Further modeling to better understand the impact of different physical mechanisms which contribute to UV spectral formation, and which observational quantities best measure this diversity are ongoing.

ACKNOWLEDGEMENTS

EB and JD are supported in part by NASA grant 80NSSC20K0538. Some of the calculations presented here were performed at the Höchstleistungs Rechenzentrum Nord (HLRN), at the National Energy Research Supercomputer Center (NERSC), which is supported by the Office of Science of the U.S. Department of Energy under Contract No. DE-AC03-76SF00098 and at the OU Supercomputing Center for Education & Research (OSCER) at the University of Oklahoma (OU). We thank all these institutions for a generous allocation of computer time. MDS and EK are supported by an Experiment grant (# 28021) from the Villum FONDEN, and by a project 1 grant (#8021-00170B) from the Independent Research Fund Denmark (IRFD). LG acknowledges financial support from the Spanish Ministerio de Ciencia e Innovación (MCIN), the Agencia Estatal de Investigación (AEI) 10.13039/501100011033, and the European Social Fund (ESF) 'Investing in your future' under the 2019 Ramón y Cajal program RYC2019-027683-I and the PID2020-115253GA-I00 HOSTFLOWS project, from Centro Superior de Investigaciones Científicas (CSIC) under the PIE project 20215AT016, and the program Unidad de Excelencia María de Maeztu CEX2020-001058-M. BJS is also supported by NSF grants AST-1907570, AST-1920392 and AST-1911074. AR acknowledges support from ANID BECAS/DOCTORADO NACIONAL 21202412. Based on observations with the NASA/ESA Hubble Space Telescope obtained at the Space Telescope Science Institute, which is operated by the Association of Universities for Research in Astronomy, Incorporated, under NASA contract NAS5-26555. Support for Program number 16221 was provided through a grant from the STScI under NASA contract NAS5-26555. This paper includes data gathered with the 6.5 m Magellan Telescopes located at Las Campanas Observatory, Chile. We thank the students of the Spring 2021 Advanced Observatory Methods class at OU, Mukremin Kilic, and the staff at Apache Point Observatory including Russet McMillan and Candace Gray for obtaining spectra of SN 2021fxy during their telescope training on 2021 April 1 and 3. Based on observations made with the Nordic Optical Telescope (NOT), operated by the Nordic Optical Telescope Scientific Association at the Observatorio del Roque de los Muchachos, La Palma, Spain, of the Instituto de Astrofisica de Canaries. Data obtained with the NOT by NUTS2 was done in part due to funds from the Instrument-center for Danish Astrophysics (IDA).

DATA AVAILABILITY

Some data underlying this article are available in the article, with other data available in its online supplementary material. Full photometry can be found in Appendix A. The spectra presented in this paper are available from the data downloads page of the POISE site. They have also been archived at WISeREP.

REFERENCES

Ashall C. et al., 2019a, ApJ, 875, L14
Ashall C. et al., 2019b, ApJ, 878, 86
Ashall C. et al., 2022, ApJ, 932, L2
Barna B. et al., 2021, MNRAS, 506, 415
Baron E., Nugent P. E., Branch D., Hauschildt P. H., 2004, ApJ, 616, L91
Benetti S. et al., 2005, ApJ, 623, 1011
Benetti S., Callis E., Fraser M., Dong S., Losada I. R., 2017, Transient Name Server Classification Report, Vol. 2017–1381. p. 1
Bloom J. S. et al., 2012, ApJ, 744, L17
Branch D., Baron E., Hall N., Melakayil M., Parrent J., 2005, PASP, 117, 545

Branch D. et al., 2006, PASP, 118, 560
Breeveld A. A., Landsman W., Holland S. T., Roming P., Kuin N. P. M., Page M. J., 2011, in McEnery J. E., Racusin J. L., Gehrels N.eds, AIP Conf. Ser. Vol. 1358, Gamma Ray Bursts. Am. Inst. Phys., New York, p. 373
Brown P., 2014, in Proc. Sci., Swift: 10 Years of Discovery (SWIFT 10). SISSA, Trieste, PoS#125
Brown P. J., Breeveld A. A., Holland S., Kuin P., Pritchard T., 2014, Ap&SS, 354, 89
Brown P. J., Landez N. J., Milne P. A., Stritzinger M. D., 2017, ApJ, 836, 232
Brown P. J. et al., 2019, ApJ, 877, 152
Bulla M. et al., 2020, ApJ, 902, 48
Burns C. R. et al., 2014, ApJ, 789, 32
Burns C. R. et al., 2018, ApJ, 869, 56
Burns C. R. et al., 2020, ApJ, 895, 118
Burns C. et al., 2021, Astron. Telegram, 14441, 1
Burrow A. et al., 2020, ApJ, 901, 154
Buton C. et al., 2013, A&A, 549, A8
Cain C. et al., 2018, ApJ, 869, 162
Childress M. J., Filippenko A. V., Ganeshalingam M., Schmidt B. P., 2014, MNRAS, 437, 338
Contreras C. et al., 2018, ApJ, 859, 24
Cushing M. C., Vacca W. D., Rayner J. T., 2004, PASP, 116, 362
DerKacy J. M., Baron E., Branch D., Hoeflich P., Hauschildt P., Brown P. J., Wang L., 2020, ApJ, 901, 86
Dessart L., Hillier D. J., 2010, MNRAS, 405, 2141
de Vaucouleurs G., de Vaucouleurs A., Corwin Herold G. J., Buta R. J., Paturel G., Fouque P., 1991, Third Reference Catalogue of Bright Galaxies. Springer, Berlin
Dimitriadis G. et al., 2019, ApJ, 870, L1
Filippenko A. V. et al., 1992, ApJ, 384, L15
Foley R. J., Kirshner R. P., 2013, ApJ, 769, L1
Foley R. J. et al., 2012, ApJ, 744, 38
Foley R. J. et al., 2016, MNRAS, 461, 1308
Foley R. J., Hoffmann S. L., Macri L. M., Riess A. G., Brown P. J., Filippenko A. V., Graham M. L., Milne P. A., 2020, MNRAS, 491, 5991
Gall C. et al., 2018, A&A, 611, A58
Garavini G. et al., 2004, AJ, 128, 387
Gordon K. D. et al., 2014, ApJ, 797, 85
Goudfrooij P., Hansen L., Jorgensen H. E., Norgaard-Nielsen H. U., 1994, A&AS, 105, 341
Graham M. L. et al., 2015, MNRAS, 446, 2073
Hachinger S. et al., 2013, MNRAS, 429, 2228
Hamuy M. et al., 2002, AJ, 124, 417
Hauschildt P. H., 1992, J. Quant. Spec. Radiat. Transf., 47, 433
Hoeflich P., Khokhlov A. M., Wheeler J. C., 1995, ApJ, 444, 831
Hoeflich P. et al., 2017, ApJ, 846, 58
Höflich P., 2006, Nucl. Phys. A, 777, 579
Höflich P., Stein J., 2002, ApJ, 568, 779
Holmbo S., 2020, Phd Thesis, Aarhus University
Hoogendam W. B. et al., 2022, ApJ, 928, 103
Hosseinzadeh G. et al., 2017, ApJ, 845, L11
Hosseinzadeh G. et al., 2022, ApJ, 933, L45
Hoyle F., Fowler W. A., 1960, ApJ, 132, 565
Hsiao E. Y. et al., 2013, ApJ, 766, 72
Hsiao E. Y. et al., 2019, PASP, 131, 014002
Iben I. J., Tutukov A. V., 1984, ApJS, 54, 335
Itagaki K., 2021, Transient Name Server Discovery Report, 2021–785. p. 1
Jeffery D. J., Branch D., 1990, in Wheeler J. C., Piran T., Weinberg S., eds, Supernovae, Jerusalem Winter School for Theoretical Physics, Vol. 6, World Scientific Publishing, Singapore, p. 149
Jeffery D. J., Leibundgut B., Kirshner R. P., Benetti S., Branch D., Sonneborn G., 1992, ApJ, 397, 304
Jha S. W., Sand D., Valenti S., Hiramatsu D., Groenewald D., 2021, Transient Name Server Classification Report, 2021–813. p. 1
Jiang J.-A. et al., 2017, Nature, 550, 80
Kasen D., 2010, ApJ, 708, 1025
Kashi A., Soker N., 2011, MNRAS, 417, 1466
Kochanek C. S. et al., 2017, PASP, 129, 104502
Krisciunas K. et al., 2017, AJ, 154, 211
Lantz B. et al., 2004, in Mazuray L., Rogers P. J., Wartmann R., eds, Proc. SPIE Conf. Ser. Vol. 5249, Optical Design and Engineering. SPIE, Bellingham, p. 146
Lentz E. J., Baron E., Branch D., Hauschildt P. H., Nugent P. E., 2000, ApJ, 530, 966
Li W. et al., 2019, ApJ, 870, 12
Livne E., Arnett D., 1995, ApJ, 452, 62
Lundqvist P. et al., 2020, ApJ, 890, 159
Maeda K., Kutsuna M., Shigeyama T., 2014, ApJ, 794, 37
Maoz D., Mannucci F., Nelemans G., 2014, ARA&A, 52, 107
Marion G. H., Höflich P., Gerardy C. L., Vacca W. D., Wheeler J. C., Robinson E. L., 2009, AJ, 138, 727
Mathis J. S., 1990, ARA&A, 28, 37
Mazzali P. A. et al., 2005, ApJ, 623, L37
Mazzali P. A. et al., 2014, MNRAS, 439, 1959
McCully C. et al., 2018, Lcogt/Banzai: Initial Release, Zenodo
Milne P. A., Brown P. J., Roming P. W. A., Bufano F., Gehrels N., 2013, ApJ, 779, 23
Milne P. A., Foley R. J., Brown P. J., Narayan G., 2015, ApJ, 803, 20
Mitchell R. C., Baron E., Branch D., Hauschildt P. H., Nugent P. E., Lundqvist P., Blinnikov S., Pun C. S. J., 2002, ApJ, 574, 293
Mould J. R. et al., 2000, ApJ, 529, 786
Nomoto K., Thielemann F. K., Yokoi K., 1984, ApJ, 286, 644
Nugent P., Phillips M., Baron E., Branch D., Hauschildt P., 1995, ApJ, 455, L147
Nugent P. E. et al., 2011, Nature, 480, 344
Pakmor R., Kromer M., Röpke F. K., Sim S. A., Ruiter A. J., Hillebrandt W., 2010, Nature, 463, 61
Pakmor R., Kromer M., Taubenberger S., Sim S. A., Röpke F. K., Hillebrandt W., 2012, ApJ, 747, L10
Pan Y. C. et al., 2015, MNRAS, 452, 4307
Pereira R. et al., 2013, A&A, 554, A27
Perlmutter S. et al., 1999, ApJ, 517, 565
Phillips M. M., 1993, ApJ, 413, L105
Phillips M. M., Wells L. A., Suntzeff N. B., Hamuy M., Leibundgut B., Kirshner R. P., Foltz C. B., 1992, AJ, 103, 1632
Phillips M. M., Lira P., Suntzeff N. B., Schommer R. A., Hamuy M., Maza J., 1999, AJ, 118, 1766
Phillips M. M. et al., 2013, ApJ, 779, 38
Phillips M. M. et al., 2019, PASP, 131, 014001
Phillips M. M. et al., 2022, ApJ, 938, 47
Pignata G. et al., 2008, MNRAS, 388, 971
Piro A. L., Morozova V. S., 2016, ApJ, 826, 96
Piro A. L., Chang P., Weinberg N. N., 2010, ApJ, 708, 598
Polin A., Nugent P., Kasen D., 2019, ApJ, 873, 84
Poznanski D., Prochaska J. X., Bloom J. S., 2012, MNRAS, 426, 1465
Rayner J. T., Toomey D. W., Onaka P. M., Denault A. J., Stahlberger W. E., Vacca W. D., Cushing M. C., Wang S., 2003, PASP, 115, 362
Riess A. G. et al., 1998, AJ, 116, 1009
Riess A. G. et al., 2022, ApJ, 934, L7
Rosswog S., Kasen D., Guillochon J., Ramirez-Ruiz E., 2009, ApJ, 705, L128
Rothberg B., Joseph R. D., 2006, AJ, 131, 185
Sai H. et al., 2022, MNRAS, 514, 3541
Sauer D. N. et al., 2008, MNRAS, 391, 1605
Schlafly E. F., Finkbeiner D. P., 2011, ApJ, 737, 103
Schlegel D. J., Finkbeiner D. P., Davis M., 1998, ApJ, 500, 525
Scolnic D. et al., 2020, ApJ, 896, L13
Shappee B. J. et al., 2014, ApJ, 788, 48
Shappee B. J. et al., 2016, ApJ, 826, 144
Shappee B. J. et al., 2019, ApJ, 870, 13
Shen K. J., Kasen D., Miles B. J., Townsley D. M., 2018, ApJ, 854, 52
Silverman J. M., Kong J. J., Filippenko A. V., 2012, MNRAS, 425, 1819
Soker N., García-Berro E., Althaus L. G., 2014, MNRAS, 437, L66
Stahl B. E. et al., 2020, MNRAS, 492, 4325
Stritzinger M. et al., 2002, AJ, 124, 2100
Stritzinger M. D. et al., 2018, ApJ, 864, L35

Sullivan M. et al., 2010, MNRAS, 406, 782
Thielemann F. K., Nomoto K., Yokoi K., 1986, A&A, 158, 17
Tody D., 1986, in Crawford D. L., ed., Proc. SPIE Conf. Ser. Vol. 627, Instrumentation in astronomy VI. SPIE, Bellingham, p. 733
Tody D., 1993, in Hanisch R. J., Brissenden R. J. V., Barnes J., eds, ASP Conf. Ser. Vol. 52, Astronomical Data Analysis Software and Systems II. Astron. Soc. Pac., San Francisco, p. 173
Tonry J. et al., 2017, Transient Name Server Discovery Report, 2017–1371. p. 1
Tucker M. A. et al., 2022, PASP, 134, 124502
van Dokkum P. G., 2001, PASP, 113, 1420
Walker E. S., Hachinger S., Mazzali P. A., Ellis R. S., Sullivan M., Gal Yam A., Howell D. A., 2012, MNRAS, 427, 103
Wang X. et al., 2009, ApJ, 699, L139
Wang X. et al., 2012, ApJ, 749, 126
Webbink R. F., 1984, ApJ, 277, 355
Whelan J., Iben Icko J., 1973, ApJ, 186, 1007
Woosley S. E., Weaver T. A., 1994, ApJ, 423, 371
Yanchulova Merica-Jones P. et al., 2021, ApJ, 907, 50

SUPPORTING INFORMATION

Supplementary data are available at *MNRAS* online.

Table S1. SN 2017erp SYNOW Parameters.
Table S2. SN 2021fxy SYNOW Parameters

Please note: Oxford University Press is not responsible for the content or functionality of any supporting materials supplied by the authors. Any queries (other than missing material) should be directed to the corresponding author for the article.

APPENDIX A: PHOTOMETRIC DATA

Table A1. Log of *Swift* photometry for SN 2021fxy.

MJD	*UVM*2 (mag)	*UVW*1 (mag)	UVW2 (mag)	*U* (mag)	*B* (mag)	*V* (mag)
59291.39	–	–	–	–	–	16.53(0.12)
59291.45	–	18.74(0.11)	–	17.24(0.007)	16.70(0.06)	–
59292.13	–	–	–	–	–	15.85(0.08)
59292.18	–	18.74(0.11)	–	16.89(0.07)	–	–
59292.19	–	–	–	–	16.12(0.06)	–
59293.37	–	17.33(0.13)	–	15.89(0.09)	15.59(0.07)	15.52(0.10)
59300.12	–	15.48(0.06)	17.07(0.09)	13.80(0.04)	14.08(0.04)	14.07(0.06)
59300.24	–	–	17.14(0.11)	–	–	–
59300.32	–	–	17.15(0.07)	–	–	–
59300.35	18.82(0.27)	–	–	–	–	–
59304.59	–	15.40(0.07)	16.81(0.10)	13.73(0.04)	13.91(0.04)	13.78(0.05)
59309.77	–	15.77(0.08)	–	14.06(0.05)	–	–
59309.78	–	–	17.22(0.20)	–	14.03(0.04)	–

Table A2. Log of optical photometry of SN 2021fxy.

MJD	*u* (mag)	*B* (mag)	*V* (mag)	*g* (mag)	*r* (mag)	*i* (mag)	Telescope
59291.12	18.54(0.04)	17.18(0.01)	16.65(0.01)	16.93(0.01)	16.66(0.01)	17.06(0.02)	Swope
59291.32	18.38(0.04)	16.97(0.01)	16.54(0.01)	16.79(0.01)	16.55(0.01)	16.93(0.02)	Swope
59294.10	16.18(0.03)	15.27(0.01)	15.16(0.01)	15.21(0.01)	15.20(0.01)	15.53(0.01)	Swope
59294.31	16.07(0.03)	15.19(0.01)	15.10(0.01)	15.13(0.01)	15.13(0.01)	15.45(0.01)	Swope
59295.11	15.69(0.03)	14.93(0.01)	14.87(0.01)	14.88(0.01)	14.90(0.01)	15.21(0.01)	Swope
59295.34	15.61(0.03)	14.81(0.01)	14.80(0.01)	14.78(0.01)	14.80(0.01)	15.11(0.01)	Swope
59295.40	15.57(0.03)	14.85(0.01)	14.78(0.01)	14.79(0.01)	14.83(0.01)	15.13(0.01)	Swope
59296.09	15.32(0.03)	14.66(0.01)	14.62(0.01)	14.62(0.01)	14.66(0.01)	14.94(0.01)	Swope
59296.27	15.25(0.03)	14.54(0.01)	14.57(0.01)	14.55(0.01)	14.61(0.01)	14.91(0.01)	Swope
59296.39	15.25(0.03)	14.56(0.01)	14.57(0.01)	14.54(0.01)	14.58(0.01)	14.87(0.02)	Swope
59297.25	15.02(0.03)	14.42(0.01)	14.41(0.01)	14.40(0.01)	14.45(0.01)	14.75(0.01)	Swope
59298.25	14.85(0.03)	14.27(0.01)	14.27(0.01)	14.24(0.01)	14.30(0.01)	14.65(0.01)	Swope
59299.11	–	14.09(0.01)	14.21(0.01)	14.15(0.01)	14.23(0.01)	–	LCOGT
59299.25	14.72(0.03)	14.17(0.01)	14.16(0.01)	14.13(0.01)	14.19(0.01)	14.56(0.01)	Swope
59300.20	14.65(0.03)	14.11(0.01)	14.08(0.01)	14.06(0.01)	14.13(0.01)	14.56(0.01)	Swope
59300.93	–	13.89(0.01)	14.03(0.01)	13.97(0.01)	14.08(0.01)	–	LCOGT
59301.19	14.59(0.03)	13.96(0.02)	14.01(0.01)	–	–	14.52(0.01)	Swope
59302.24	14.55(0.03)	13.96(0.01)	13.94(0.01)	13.94(0.01)	14.02(0.01)	14.56(0.01)	Swope
59303.19	14.54(0.03)	13.93(0.01)	13.92(0.01)	13.90(0.01)	13.97(0.01)	14.55(0.02)	Swope
59304.23	14.58(0.03)	13.93(0.01)	13.90(0.01)	13.90(0.01)	13.95(0.01)	14.60(0.01)	Swope
59305.25	14.57(0.03)	13.95(0.01)	13.90(0.01)	13.89(0.01)	13.94(0.01)	14.62(0.01)	Swope

Table A2 – *continued*

MJD	*u* (mag)	*B* (mag)	*V* (mag)	*g* (mag)	*r* (mag)	*i* (mag)	Telescope
59306.16	14.63(0.03)	13.93(0.01)	13.89(0.01)	13.88(0.01)	13.91(0.01)	14.63(0.01)	Swope
59307.14	14.68(0.03)	13.97(0.01)	13.91(0.01)	13.90(0.01)	13.94(0.01)	14.67(0.01)	Swope
59309.26	14.81(0.03)	14.03(0.01)	13.95(0.01)	13.96(0.01)	13.96(0.01)	14.72(0.01)	Swope
59310.21	14.89(0.03)	14.08(0.01)	13.98(0.01)	14.00(0.01)	14.01(0.01)	14.78(0.01)	Swope
59311.23	14.96(0.03)	14.04(0.01)	13.96(0.01)	14.01(0.01)	14.01(0.01)	14.77(0.01)	Swope
59312.30	15.10(0.05)	14.21(0.02)	14.04(0.01)	14.09(0.01)	14.10(0.01)	14.85(0.01)	Swope
59312.30	15.14(0.08)	14.21(0.02)	14.04(0.01)	14.09(0.01)	14.10(0.01)	14.85(0.01)	Swope
59313.23	15.14(0.03)	14.20(0.01)	14.06(0.01)	14.11(0.01)	14.12(0.01)	14.91(0.01)	Swope
59313.46	–	14.24(0.01)	14.13(0.01)	14.20(0.01)	14.21(0.01)	–	LCOGT
59314.23	15.26(0.03)	14.36(0.01)	14.13(0.01)	14.21(0.01)	14.23(0.01)	15.01(0.01)	Swope
59315.06	15.32(0.03)	14.41(0.01)	14.18(0.01)	14.26(0.01)	14.30(0.01)	15.08(0.01)	Swope
59316.29	15.50(0.03)	14.49(0.01)	14.24(0.01)	14.32(0.01)	14.36(0.01)	15.13(0.01)	Swope
59317.23	15.62(0.03)	14.52(0.01)	14.28(0.01)	14.37(0.01)	14.42(0.01)	15.22(0.01)	Swope
59324.29	–	–	14.74(0.01)	15.07(0.01)	14.76(0.01)	15.23(0.01)	LCOGT
59325.85	–	15.53(0.01)	14.82(0.01)	15.18(0.01)	14.75(0.01)	15.14(0.01)	LCOGT
59337.42	–	16.55(0.02)	15.59(0.01)	16.21(0.01)	15.28(0.01)	15.31(0.01)	LCOGT
59342.27	–	16.84(0.03)	15.84(0.02)	16.48(0.01)	15.57(0.01)	15.67(0.02)	LCOGT
59345.72	–	16.89(0.02)	16.00(0.01)	16.55(0.01)	15.75(0.01)	15.84(0.01)	LCOGT
59350.71	–	17.05(0.02)	16.10(0.01)	16.67(0.01)	15.93(0.01)	16.07(0.01)	LCOGT
59352.79	–	17.08(0.01)	16.18(0.01)	16.75(0.01)	15.99(0.01)	16.16(0.01)	LCOGT
59361.82	–	17.12(0.10)	16.37(0.05)	16.92(0.03)	16.29(0.01)	16.35(0.09)	LCOGT
59364.74	–	17.29(0.02)	16.48(0.01)	16.93(0.01)	16.38(0.01)	16.61(0.02)	LCOGT
59365.58	–	17.31(0.02)	16.53(0.01)	16.97(0.01)	16.43(0.01)	16.67(0.01)	LCOGT
59374.89	–	17.39(0.02)	16.76(0.02)	17.10(0.01)	16.69(0.01)	16.94(0.02)	LCOGT

APPENDIX B: SYNOW FITS OF SN 2021FXY

SYNOW is a highly parametrized code designed to simulate supernova spectra, to assist in the identification of spectral lines and estimation of the both photospheric velocity and velocity interval of ions within the supernova ejecta. It makes simple assumptions about the supernova, including spherical symmetry, homologous expansion, line formation via resonance scattering in the Sobolev approximation, and a sharp photosphere emitting a blackbody continuum to calculate a synthetic spectra. Key user defined parameters include the temperature of the blackbody continuum, photospheric velocity, and the reference line optical depth, e-folding velocity, velocity extent, and the Boltzmann excitation temperature for each ion included in the fit. The best-fitting spectrum is then determined via 'chi-by-eye', as is the community standard. More information on SYNOW can be found in Jeffery & Branch (1990) and Branch et al. (2005, 2006).

As stated above, SNe 2021fxy and 2017erp show numerous similarities. Both have suppressed flux in the mid-UV and show features that are nearly identical in velocity, line profile, and line depth. However, SN 2021fxy evolves through its photospheric phase faster than 2017erp, as measured by the Si II λ6355 line, and the two SNe are members of different Branch groups. Using SYNOW, we can investigate just how similar the ejecta of the two SNe are.

Our generalized fitting procedure is as follows. After assuming a blackbody temperature T_{bb}, we fit the Si II features, assuming that the photospheric velocity ($v_{\rm phot}$) is the same as the $v_{\rm min}$ of Si II. With the PV established, we fit ions of other IMEs, including Ca II, S II, Mg II, etc., including any HV components. Once initial fits of the IMEs are complete, we add the important ions arising from the IGEs, including Fe II, Fe III, Co II, and Ni II, revising our IME parameters as necessary to fit blended features. We assume an excitation temperature of ($T_{\rm exec}$ = 10 000 K) unless stated otherwise. The full set of input parameters are listed in Tables B1 and B2. Our complete set of fits to both SNe 2017erp and 2021fxy are found in Fig. B1, with a representative example of the single-ion fits shown for the −5.9-d spectrum of SN 2021fxy in Fig. B2. We briefly summarize our important findings below.

As previously shown in Fig. 17, several epochs of SN 2021fxy show broad, flat-topped emission profiles characteristic of line formation occurring in a region detached from the photosphere (Jeffery & Branch 1990). However, because of our assumption that $v_{\rm phot} = v_{\rm min,\,Si}$, we only find one epoch of SN 2021fxy where Si II

Table B1. SN 2017erp SYNOW parameters.

Ion	Parameter	−17.0 d	−14.1 d	−8.5 d	−1.0 d	0.0 d	+6.0 d	+11.4 d
	$T_{\rm bb}$ (K)	10 500	10 500	9500	11 000	11 000	10 000	9800
	$v_{\rm phot}$ (10^3 km s^{-1})	15.0	13.9	12.5	11.0	11.0	9.8	8.5
	$v_{\rm max}$ (10^3 km s^{-1})	45.0	45.0	35.0	30.0	25.0	25.0	25.0
C II	τ	–	0.14	–	–	–	–	–
	$v_{\rm min}/v_{\rm max}$	–	13.9/25.0	–	–	–	–	–
	$v_{\rm e}$	–	2.0	–	–	–	–	–
	$T_{\rm exec}$	–	20000	–	–	–	–	–

Note. The full table of SYNOW parameters for the SN 2017erp fits shown in Fig. B1 are available online as supplemental material.

Table B2. SN 2021fxy SYNOW parameters.

Ion	Parameter	−13.9 d	−5.9 d	+1.3 d	+3.2 d	+5.1 d	+10.9 d
C II	T_{bb} (K)	10 500	13 000	13 000	12 000	15 000	9300
	v_{phot} (10^3 km s^{-1})	15.0	10.8	10.0	10.0	9.0	8.0
	v_{max} (10^3 km s^{-1})	40.0	30.0	25.0	25.0	25.0	25.0
	τ	0.18	–	–	–	–	–
	v_{min}/v_{max}	15.0/25.0	–	–	–	–	–
	v_e	2.0	–	–	–	–	–
	T_{exec}	17000	–	–	–	–	–

Note. The full table of SYNOW parameters for the SN 2021fxy fits shown in Fig. B1 are available online as supplemental material.

is clearly detached. Most likely, the Si II in the preceding epochs is detached by $\lesssim$1000 km s^{-1}, as this represents the 3σ error in our velocity measurements. This is supported by the appearance of a weak C IIλ6580 line at +5.1 d in SN 2021fxy, which serves to further flatten the emission peak. We find further support for this idea by examining the Si III lines, which is also detached from the photosphere at +5.1 d. As none of the Si lines in the SN 2017erp fits are detached, our SYNOW fits support our finding that SN 2021fxy evolves through its photospheric phase faster than SN 2017erp.

The Ca II lines proved particularly difficult to fit well. In addition to many of the NIR triplet features showing flat-topped emission peaks similar to the Si II lines, both the H&K lines and the NIR triplets often required multiple detached or HV components to accurately represent the feature. We were able to distinguish the different HV components through their different v_{max} values. These narrow regions may be indications of a series of shells in the outer layers of the SNe ejecta. Yet, the numerous components often resulted in fits that were not able to reproduce both features accurately. In SN 2021fxy, we were able to obtain good fits to both the Ca II features in all epochs except +1.3 and +10.9 d, where the NIR triplet is preferentially fit. For SN 2017erp, the NIR triplet is preferentially fit in the −17.0 and −14.1 d spectra due to incomplete coverage of the H&K features, and is preferentially fit in the −8.5 and −1.0-d spectra.

S II lines are present from the earliest epochs in both SNe. The features grow stronger in both SNe, peaking in strength near maximum light before weakening significantly by ∼+11 d. The strength of S II is correlated with the photospheric temperature; however, the response is both non-monotonic and strongly influenced by NLTE effects (Nugent et al. 1995). Therefore, although the excitation temperatures of the S II lines increase in both SNe, also peaking near maximum light it is difficult to discern whether this accurately captures the physics. C II lines are also present in the early epochs of both SNe. We find agreement with Brown et al. (2019) that the C II lines are present at early times in SN 2017erp, but disappear in our fits after ∼−10 d. We similarly find evidence for a weak C II line in the −13.9-d spectra of SN 2021fxy, which disappears before our next spectrum at −5.9 d. Both SNe show features at the expected location of the O I λ7773 line, yet the contamination of this feature by telluric lines and a strong contribution of Mg II λλ7896, 7877 doublet (likely overemphasized by our SYNOW fit) in SN 2021fxy makes fitting difficult. As a result, we can only definitively identify O I in the +5.1-d spectrum. In order to fit the blue Mg II features in SNe 2021fxy and 2017erp, our fits require that the Mg II be located at high velocities and/or have high excitation temperatures, resulting in the high excitation lines at λλ7896, 7877 appearing abnormally strong at the location of the O I lines. Examination of the NIR spectra of SN 2021fxy reveals Mg II lines that are weaker than those found in other NIR spectra of other SNe Ia, likely caused by the MUV suppression preventing the UV photons from exciting the upper states of Mg II. However, it is interesting to note that Barna et al. (2021) also find evidence for Mg II at high velocities in their fit of ASASSN-14lp. Further investigation of the connection between HV Mg and MUV suppressed SNe Ia is warranted.

At early times, the influence of IGEs on the spectra is restricted to HV and PV components of Fe II and Fe III. In SN 2017erp, Fe III is photospheric at all epochs except −17.0 d, while Fe II is consistently found as a high velocity feature. In SN 2021fxy; however, the HV Fe III persists until at least the −5.9-d spectrum, while a weak photospheric component of Fe II begins appearing as early as −5.9 d. At later epochs, the influence of Ni II and Co II on the spectra become stronger, as the photosphere recedes into the Fe-rich inner regions of the ejecta.

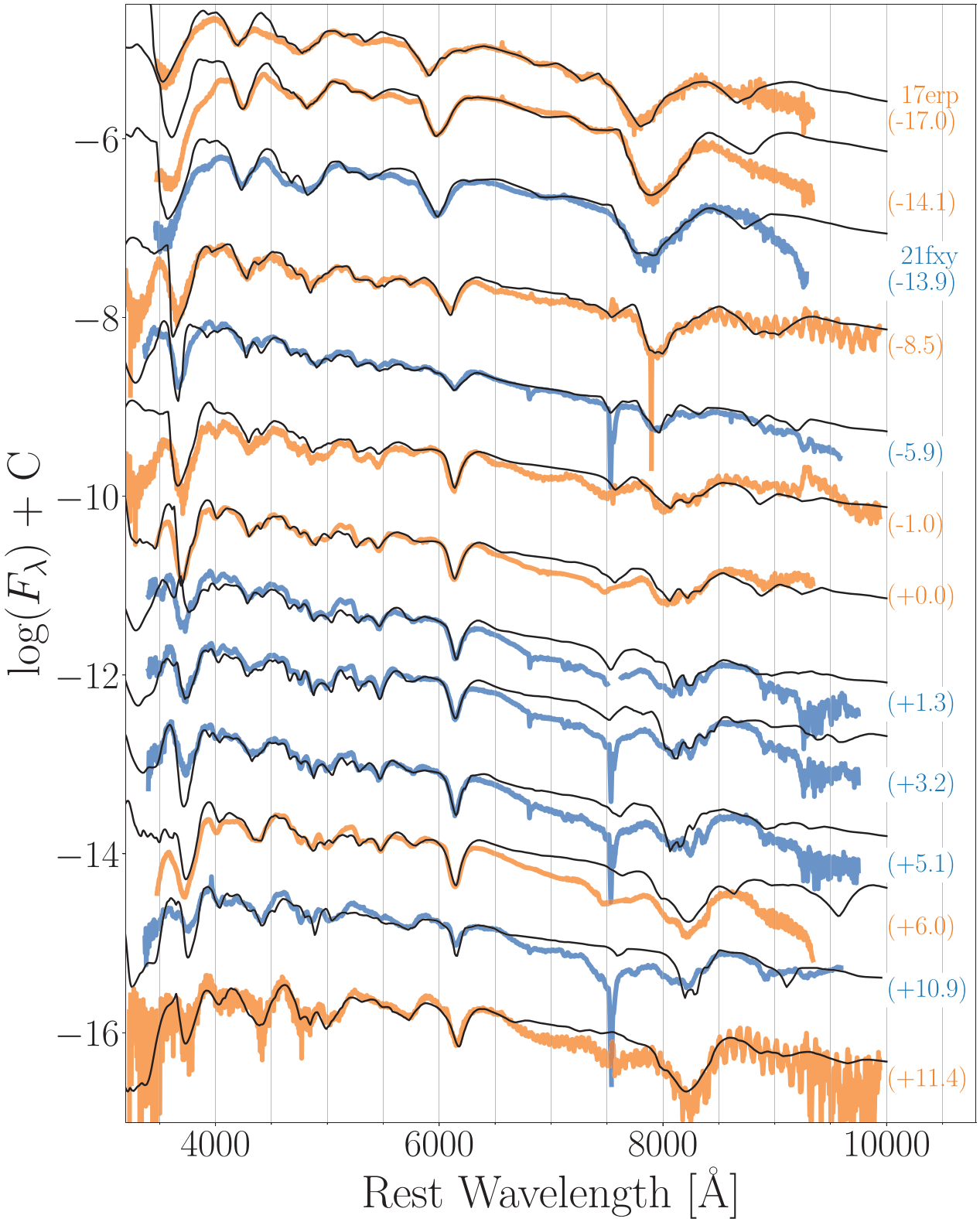

Figure B1. Optical sequences of SN 2017erp (orange) and SN 2021fxy (blue), with SYNOW fits overlaid in black.

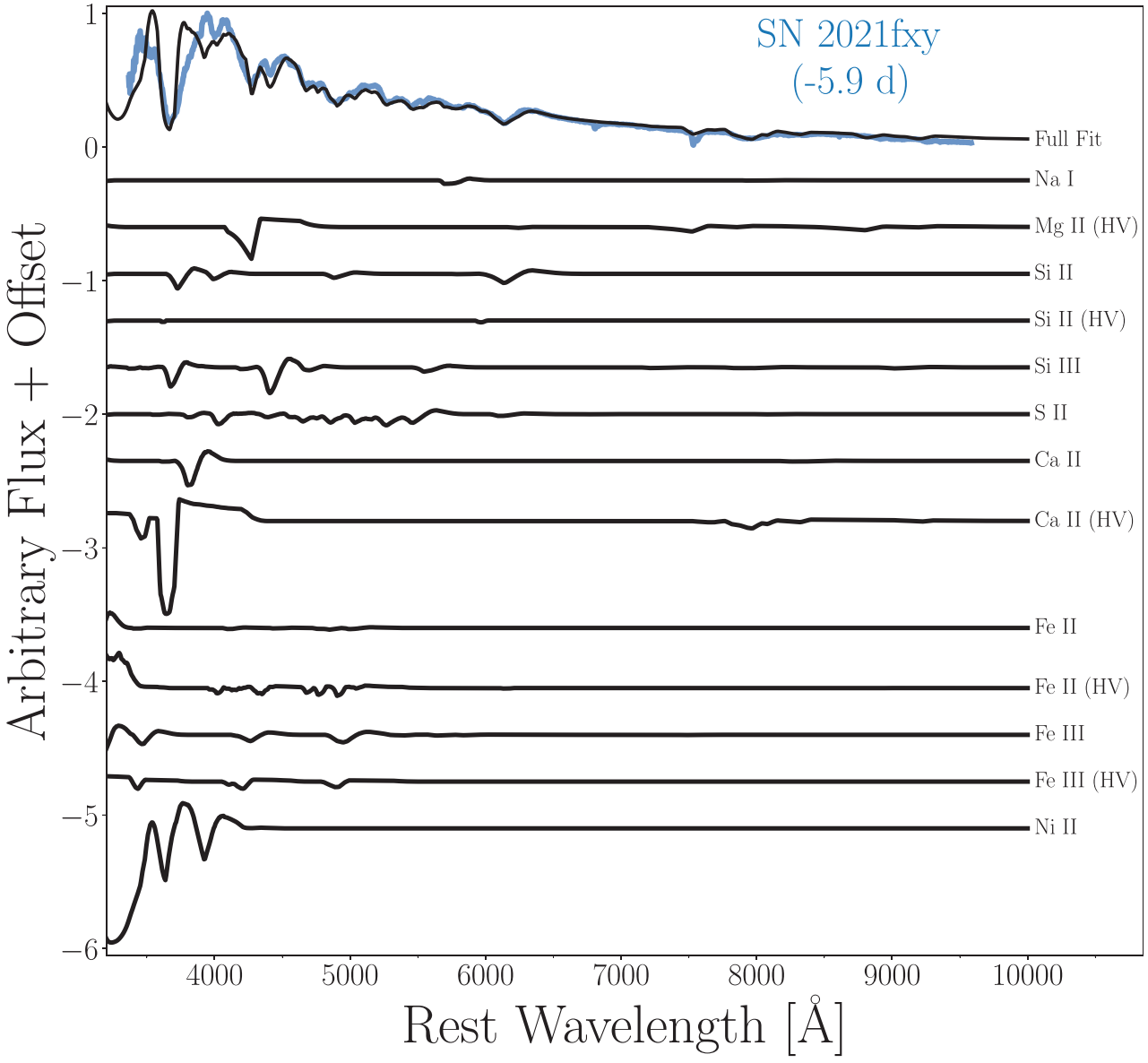

Figure B2. Continuum normalized single-ion fits to the −5.9-d spectrum of SN 2021fxy (blue), with the complete best fitting model overlaid in black.

[1]*Homer L. Dodge Department of Physics and Astronomy, University of Oklahoma, 440 W. Brooks, Norman, OK 73019-2061, USA*
[2]*Department of Physics, Virginia Tech, 850 West Campus Drive, Blacksburg, VA 24061, USA*
[3]*Planetary Science Institute, 1700 East Fort Lowell, Suite 106, Tucson, AZ 85719-2395 USA*
[4]*Hamburger Sternwarte, Gojenbergsweg 112, D-21029 Hamburg, Germany*
[5]*George P. and Cynthia Woods Mitchell Institute for Fundamental Physics and Astronomy, Department of Physics and Astronomy, Texas A&M University, College Station, TX 77843, USA*
[6]*The Observatories of the Carnegie Institution for Science, 813 Santa Barbara Street, Pasadena, CA 91101, USA*
[7]*Department of Physics, Florida State University, 77 Chieftan Way, Tallahassee, FL 32306, USA*
[8]*Carnegie Observatories, Las Campanas Observatory, Casilla 601, La Serena, Chile*
[9]*Space Telescope Science Institute, 3700 San Martin Drive, Baltimore, MD 21218-2410, USA*
[10]*Institute for Astronomy, University of Hawaii, 2680 Woodlawn Drive, Honolulu, HI 96822, USA*
[11]*Department of Physics and Astronomy, Aarhus University, Ny Munkegade 120, DK-8000 Aarhus C, Denmark*
[12]*CCAPP Fellow, Center for Cosmology and Astroparticle Physics, The Ohio State University, 191 West Woodruff Ave, Columbus, OH 43210, USA*
[13]*Department of Astronomy, The Ohio State University, 140 West 18th Avenue, Columbus, OH 43210, USA*
[14]*Department of Physics, The Ohio State University, 191 West Woodruff Ave, Columbus, OH 43210, USA*
[15]*Department of Physics & Astronomy, Louisiana State University, Baton Rouge, LA 70803, USA*
[16]*Institute of Space Sciences (ICE, CSIC), Campus UAB, Carrer de Can Magrans s/n, E-08193 Barcelona, Spain*
[17]*Institut d'Estudis Espacials de Catalunya (IEEC), E-08034 Barcelona, Spain*
[18]*Astrophysics Research Institute, Liverpool John Moores University, IC2, Liverpool Science Park, 146 Brownlow Hill, Liverpool L3 5RF, UK*

[19]*European Centre for Theoretical Studies in Nuclear Physics and Related Areas (ECT∗), Fondazione Bruno Kessler, I-38122 Trento, Italy*
[20]*INFN-TIFPA, Trento Institute for Fundamental Physics and Applications, Via Sommarive 14, I-38123 Trento, Italy*
[21]*INAF – Osservatorio Astronomico di Padova, Vicolo dell'Osservatorio 5, I-35122 Padova, Italy*
[22]*Finnish Centre for Astronomy with ESO (FINCA), University of Turku, FI-20014 Turku, Finland*
[23]*Tuorla Observatory, Department of Physics and Astronomy, University of Turku, FI-20014 Turku, Finland*
[24]*Oskar Klein Centre, Department of Astronomy, Stockholm University, Albanova University Centre, SE-106 91 Stockholm, Sweden*
[25]*Instituto de Astrofisica – Universidad Andres Bello, Avda. República 252, 8320000 Santiago, Chile*
[26]*Millennium Institute of Astrophysics, Nuncio Monsenor Sótero Sanz 100, Providencia, 8320000 Santiago, Chile*

This paper has been typeset from a TEX/LATEX file prepared by the author.